J. Fluid Mech. (2024), *vol*. 997, A23, doi:10.1017/jfm.2024.804

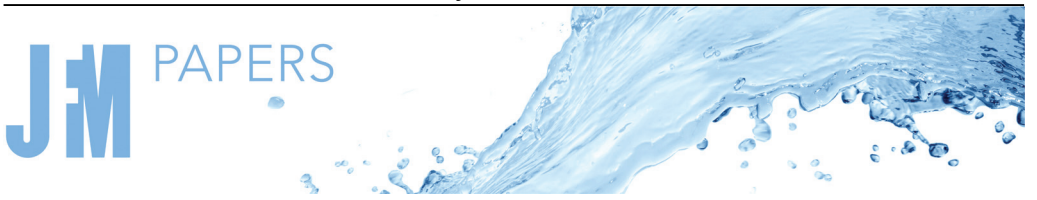

Global stability analysis of hydrodynamic focusing in the presence of a soluble surfactant

M. Rubio[1], **M.G. Cabezas**[2], **J.M. Montanero**[2,†] **and M.A. Herrada**[3]

[1]Departamento de Ingeniería Energética y Fluidomecánica and Instituto de las Tecnologías Avanzadas de la Producción (ITAP), Universidad de Valladolid, E-47003 Valladolid, Spain

[2]Departamento de Ingeniería Mecánica, Energética y de los Materiales and Instituto de Computación Científica Avanzada (ICCAEx), Universidad de Extremadura, E-06071 Badajoz, Spain

[3]Departamento de Ingeniería Aeroespacial y Mecánica de Fluidos, Universidad de Sevilla, E-41092 Sevilla, Spain

(Received 9 January 2024; revised 30 April 2024; accepted 25 June 2024)

We numerically study the influence of a soluble surfactant on the microjetting mode of the liquid–liquid flow focusing configuration. The surfactant adsorbs on the interface next to the feeding capillary and accumulates in front of the emitted jet, significantly lowering the surface tension there. The resulting Marangoni stress substantially alters the balance of the tangential stresses at the interface but does not modify the interface velocity. The global stability analysis at the minimum flow rate stability limit shows that the Marangoni stress collaborates with soluto-capillarity to stabilize the microjetting mode. Our analysis unveils the noticeable effect of the Marangoni stress associated with the surface tension perturbation. Surfactant diffusion and desorption hardly affect the stability limit. Transient numerical simulations show how subcritical and supercritical base flows respond to a spatially localized initial perturbation. Our parametric study indicates that the minimum flow rate ratio depends on the adsorption constant and the surfactant concentration through the product of these two variables. The surfactant stabilizing effect increases with the outer stream flow rate. We show that surfactants not only stabilize the microemulsion resulting from the jet breakup in hydrodynamic focusing, but also allow for the reduction of droplet size. Our findings advance the fundamental understanding of the complex role of surfactants in tip streaming via hydrodynamic focusing. In particular, our results contradict the common assumption that adding surfactant favours tip streaming simply because it reduces the meniscus tip surface tension.

Key words: capillary flows, microfluidics, multiphase flow

† Email address for correspondence: jmm@unex.es

1. Introduction

Surfactants produce many beneficial effects, such as stabilizing emulsions and foams by hindering the coalescence of droplets and bubbles (Rosen 2004) or keeping the desired wetting conditions in various microfluidic applications (Baret 2012). The major mechanical effect of a surfactant monolayer is probably the so-called soluto-capillarity effect, i.e. the local reduction of the capillary pressure due to the accumulation of surfactant molecules at an interface point. When the surfactant surface concentration is not homogeneous over the interface, the surface tension gradient causes Marangoni stress, which also plays a fundamental role in many hydrodynamic processes (Anna 2016). Marangoni stress becomes relevant in interfacial microflows, characterized by high surface-to-volume ratios.

It is worth noting that, although surface rheology (Langevin 2014; Zell *et al.* 2014) plays a secondary role in our analysis, this effect can also become important when large velocity gradients arise in viscous surfactant monolayers. This occurs, for instance, in the tip streaming of a surfactant-loaded drop driven by an extensional flow (Herrada *et al.* 2022). Surface viscous stresses also affect the linear stability (Li & Manikantan 2024) and nonlinear breakup (Martínez-Calvo & Sevilla 2020; Wee *et al.* 2020) of jets. For instance, they cause the exponential thinning of the liquid thread right before the breakup of a jet flooded by surfactant (Martínez-Calvo & Sevilla 2020) or in the limit of zero Péclet number (Wee *et al.* 2020).

Tiny fluid entities such as drops, bubbles, emulsions and capsules possess enormous relevance for a great variety of technological applications in very diverse fields, including medicine, bioengineering, industrial engineering and pharmaceutical and food industries. Several microfluidic techniques have been proposed to produce those entities (Christopher & Anna 2007). The tip streaming (Montanero & Gañán-Calvo 2020) phenomenon has been preferred for this purpose on many occasions due to its valuable capability for fabricating quasi-monodisperse collections of drops, bubbles and capsules with sizes much smaller than any characteristic length of the microfluidic device. Tip streaming occurs under relatively rare conditions because it results from a delicate balance between the forces driving and opposing the flow (Montanero & Gañán-Calvo 2020).

In liquid–liquid hydrodynamic focusing (Gañán-Calvo & Riesco-Chueca 2006; Gañán-Calvo *et al.* 2007), tip streaming is achieved by transferring energy from an outer continuous stream to the inner dispersed phase when crossing a discharge (focusing) orifice, nozzle or tube. The outer phase moves much faster than the inner one, resulting in a hydrostatic pressure drop and viscous drag. These forces collaborate in gently shaping a steady converging 'fluid nozzle' (the tapering fluid meniscus). In the microjetting mode, the meniscus tip emits a much thinner jet than the tube that feeds the dispersed phase and the discharge orifice. The jet breaks into droplets downstream due to the capillary instability (Rayleigh 1878; Tomotika 1935), giving rise to a relatively monodisperse microemulsion.

Several microfluidic configurations have been proposed to implement the hydrodynamic focusing principle in liquid–liquid systems. Salient examples are selective withdrawal (Cohen *et al.* 2001) and confined selective withdrawal (He *et al.* 2019), where the focusing phenomenon is caused by a cylindrical tube located in front of a liquid film and meniscus, respectively. The coflowing configuration (Suryo & Basaran 2006; Marín, Campo-Cortés & Gordillo 2009; Rubio-Rubio, Sevilla & Gordillo 2013; Gordillo, Sevilla & Campo-Cortés 2014) can produce a similar effect without a focusing orifice. Gañán-Calvo & Riesco-Chueca (2006) studied the steady microjetting regime arising when a liquid stream is flow focused with an outer liquid current crossing a cylindrical

orifice. Cabezas *et al.* (2021) have recently analysed numerically and experimentally the liquid–liquid flow focusing in a converging–diverging nozzle.

In most microjetting realizations, the jet's kinetic energy per unit volume $\rho_j v_j^2/2$ (ρ_j and v_j are the jet's density and velocity, respectively) is essentially independent of the injected disperse-phase flow rate Q_i. This implies that the jet diameter $d_j \sim (Q_i/v_j)^{1/2}$ scales approximately as $Q_i^{1/2}$. In principle, the jet diameter can be indefinitely reduced by lowering the injected flow rate Q_i. However, the flow inevitably becomes unstable at a minimum value of Q_i, which sets a minimum value of the jet diameter and, therefore, of the droplets resulting from its breakup (Montanero & Gañán-Calvo 2020). This occurs not only in the liquid–liquid flow focusing analysed in the present work, but also in the microjetting modes of gravitational jets (Rubio-Rubio *et al.* 2013), gaseous flow focusing (Cruz-Mazo *et al.* 2017), confined selective withdrawal (Evangelio, Campo-Cortés & Gordillo 2016; López *et al.* 2022) and electrospray (Ponce-Torres *et al.* 2018). The only exception is probably the microjetting produced by a uniaxial extensional flow under specific conditions (Rubio *et al.* 2024). Understanding the mechanisms responsible for this minimum flow rate stability limit is of great relevance both at fundamental and practical levels.

Soluble surfactants are expected to affect the stability of the tip streaming produced by flow focusing and the outcome of that flow. Surfactant molecules dissolved in the disperse phase are convected from a reservoir towards the interface, which essentially behaves as a sink of surfactant molecules due to the adsorption process. The focusing stream drags the surface elements toward the tip of the tapering meniscus, accumulating surfactant molecules in that region. The surface tension reduction in the meniscus tip is expected to enhance the tip streaming.

Large surfactant concentrations are required to produce a significant effect due to the relatively small residence time of a surface element in the tapering meniscus. López *et al.* (2022) observed experimentally that surfactants dissolved in the inner liquid of confined selective withdrawal at higher concentrations than the critical micelle concentration significantly reduced the minimum flow rate for tip streaming and the droplet diameter. The surfactant monolayer stabilized the meniscus and promoted the transition from microdripping to microjetting.

The surfactant effects have also been studied in suspended droplets (De Bruijn 1993; Eggleton, Tsai & Stebe 2001; Herrada *et al.* 2022) and bubbles (Booty & Siegel 2005) subject to extensional and shear flows, two-dimensional flow focusing (Anna, Bontoux & Stone 2003; Lee, Walker & Anna 2011; Moyle, Walker & Anna 2012) and selective withdrawal (Cohen 2004). Numerical simulations show how adding a surfactant to the inner dispersed phase produces a narrow tip streaming thread in extensional flow (Wang, Siegel & Booty 2014) and flow focusing (Wrobel *et al.* 2018). Lytra, Vlachomitrou & Pelekasis (2024) have recently proposed a finite element method to study the steady two-phase core–annular flow in a flow focusing device. Their model neglects bulk surfactant transport for certain specific parameter conditions. A local spatial stability analysis of the base flow was conducted to study the growth of interface oscillations in the downstream region.

Local stability analysis is not an accurate method to predict the parameter conditions for the instability of steady jetting via tip streaming due to the complex spatial structure of this flow. Global stability analysis (Theofilis 2011) has emerged as a valuable tool for this purpose. It unveils the mechanisms responsible for the instability by identifying the critical small amplitude (linear) perturbation destabilizing the steady base flow. Characteristics of the critical mode, such as the resulting interface perturbation, allow one to determine the

region where instability originates and how it leads to the atomization mode adopted by the system following the microjetting regime destabilization.

In the absence of surfactant, López *et al.* (2022) showed that the microjetting regime produced with confined selective withdrawal becomes unstable at the minimum flow rate stability limit due to the growth of an oscillatory perturbation (a supercritical Hopf bifurcation) affecting the tapering meniscus. The global stability analysis accurately predicted the critical flow rate ratio, the appearance of the microdripping mode and the droplet emission frequency in that mode. The global stability of flow focusing in a converging–diverging nozzle (Cabezas *et al.* 2021) showed the existence of a parameter island within which microjetting is stable under small amplitude perturbations. Oscillatory and non-oscillatory instabilities delimit this island. The unstable perturbations can originate in the tapering meniscus or beyond the discharge orifice, depending on the values of the viscosity and flow rate ratios.

This paper will extend our previous numerical stability analysis (Cabezas *et al.* 2021) to describe the surfactant influence on the microjetting mode produced by flow focusing. This extension involves all the potentially relevant effects: the surfactant diffusion in the inner-phase bulk, the adsorption–desorption kinetics, the transport of surfactant molecules over the interface and the resulting soluto-capillarity and Marangoni convection. We will study how the surfactant monolayer alters the base (steady) flow in the microjetting regime for a reference realistic parameter configuration. We will analyse the surfactant effect on the microjetting stability for that configuration. A novel aspect of this analysis will be the study of the surfactant influence on the microjetting stability through the separate effect on the base flow and the perturbations. Transient numerical simulations will show how subcritical and supercritical base flows respond to an initial perturbation. Finally, we will determine the influence of the surfactant parameters on the stability limit.

The paper is organized as follows. The problem is formulated in § 2. Section 3 presents the governing equations and briefly describes the numerical method. Sections 4 and 5 analyse the influence of the surfactant on the base flow and its stability for a reference case, respectively. Transient numerical simulations for that reference case are shown in § 6. The parametric study is shown in § 7. The paper closes with concluding remarks in § 8.

2. Formulation of the problem

2.1. *Microjetting in liquid–liquid flow focusing*

This paper analyses the effect of a soluble surfactant on the stability of the liquid–liquid hydrodynamic focusing configuration sketched in figure 1, commonly referred to as flow focusing. In this axisymmetric configuration, a liquid of density ρ_i and viscosity μ_i is injected at a constant flow rate Q_i across a cylindrical feeding capillary of radius $\hat{R}_c$. This liquid flows surrounded by an outer liquid current of density ρ_o and viscosity μ_o, immiscible with the former. The outer current is injected at a constant flow rate Q_o across a converging nozzle concentric with the inner one. The inner and outer phases coflow through the nozzle, which ends in a tube with diameter $\hat{D}$. The surface tension without surfactant is $\hat{\gamma}_*$. As explained below, we will use this value as the characteristic surface tension $\hat{\gamma}_c$.

Under certain parameter conditions, the system adopts the microjetting mode of tip streaming (Montanero & Gañán-Calvo 2020). In this mode, a jet with a diameter much smaller than $2\hat{R}_c$ and $\hat{D}$ is emitted from the tip of the fluid meniscus attached to the feeding capillary. The jet and the outer stream coflow through the discharge tube (figure 1). The jet is expected to break up into droplets beyond the fluid domain considered in our

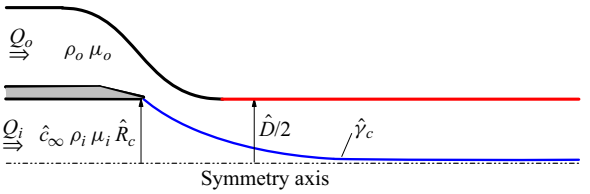

Figure 1. Sketch of the fluid configuration.

analysis. The stability of microjetting in a similar flow focusing configuration was studied by Cabezas *et al.* (2021) both experimentally and numerically. The results of the global stability analysis were in good agreement with the experiments.

The geometry considered in the present work is the same as that analysed by Cabezas *et al.* (2021) except that it incorporates a discharge cylindrical tube (marked with a red line in figure 1) not considered in that work. In this way, the inner and outer streams do not slow down beyond the nozzle neck. Perturbations growing in the tube are convected downstream. This eliminates the unstable modes associated with the jet (absolute instability) (Huerre & Monkewitz 1990) and allows one to focus on the meniscus stability. It is known that tip streaming instability originates in the tapering meniscus in most relevant realizations (Montanero & Gañán-Calvo 2020). Therefore, the stability limit for the present configuration is not expected to differ significantly from that of the geometrical configuration analysed by Cabezas *et al.* (2021). As shown in § 4, the flow fully develops near the tube entrance. For this reason, the spectrum of eigenvalues characterizing the linear dynamics becomes practically insensitive to the tube length for relatively small values of this parameter.

The geometry studied in this work can be regarded as a hybrid between flow focusing and confined selective withdrawal (He *et al.* 2019), where the focusing effect is produced by a cylindrical tube located in front of the feeding capillary. There are, however, noticeable differences between these two configurations. The shape of the focusing element (either an orifice or a tube) significantly affects the microjetting stability (López *et al.* 2022).

2.2. *The surfactant*

This paper examines the effect of a surfactant dissolved in the inner phase on the microjetting stability. The surfactant transport across the bulk is described in terms of the diffusion coefficient $\hat{\mathcal{D}}_i$. In particular, the diffusion flux normal to the interface is

$$\hat{\mathcal{J}}_{\mathcal{D}} = -\hat{\mathcal{D}}_i \frac{\partial \hat{c}}{\partial n}, \tag{2.1}$$

where $\hat{c}$ is the bulk surfactant concentration, n is the direction normal to the interface and $\partial \hat{c}/\partial n$ is evaluated at the interface (the interface sublayer). The diffuse layer also depends on the ionic strength of ionic surfactants, such as sodium dodecyl sulphate (SDS). This effect is not considered in our analysis.

We adopt the kinetic model for the adsorption/desorption flux

$$\hat{\mathcal{J}} = \hat{\mathcal{J}}_a - \hat{\mathcal{J}}_d, \quad \hat{\mathcal{J}}_a = \hat{k}_a \hat{c}_s \left(1 - \frac{\hat{\Gamma}}{\hat{\Gamma}_\infty}\right), \quad \hat{\mathcal{J}}_d = \hat{k}_d \hat{\Gamma}, \tag{2.2a–c}$$

where $\hat{\mathcal{J}}$ is the net sorption flux, $\hat{\mathcal{J}}_a$ and $\hat{\mathcal{J}}_d$ are the adsorption and desorption fluxes, respectively, $\hat{k}_a$ and $\hat{k}_d$ are the adsorption and desorption constants, respectively, $\hat{c}_s$ is the bulk surfactant concentration $\hat{c}$ evaluated at the interface, $\hat{\Gamma}$ is the surfactant surface concentration (the surface coverage, measured in mols per unit area) and $\hat{\Gamma}_\infty$ is the maximum packing density.

The surfactant molecules absorbed on the interface are transported by convection and diffusion. The surfactant surface diffusion is determined by the surface diffusion coefficient $\hat{\mathcal{D}}_s$, which typically takes values similar to those of the bulk diffusion coefficient $\hat{\mathcal{D}}_i$ (Tricot 1997).

We assume that the transfer of surfactant between the sublayer next to the interface and the interface occurs only in the form of monomers. This implies that $\hat{c}$ is the volumetric concentration of monomers even if the surfactant concentration exceeds the critical micelle concentration $\hat{c}_{cmc}$ and, therefore, there are micelles in the inner liquid. Since the micelles do not contribute to $\hat{c}_s$, values of $\hat{c}_s$ exceeding the critical micelle concentration correspond to higher experimental values of the surfactant concentration. We will consider surfactant concentrations larger than $\hat{c}_{cmc}$. However, these concentrations will be sufficiently small for the dynamical effects of the micelles to be negligible.

The surfactant is convected throughout the incompressible inner liquid phase. For this reason, the surfactant concentration in the feeding capillary is approximately the same as that in the reservoir, $\hat{c}_\infty$. The bulk diffusion coefficient $\hat{\mathcal{D}}_i$ corresponds to very high values of the Péclet number in most experiments. This implies that the bulk surfactant concentration is almost uniform in the inner phase, except within a thin diffusive layer of thickness $\hat{\lambda}_D$ next to the interface.

As shown in § 4, $\hat{\lambda}_D/\hat{R}_c \sim 10^{-3}$ for the values of $\hat{\mathcal{D}}_i$, $\hat{k}_a$ and $\hat{R}_c$ of the reference case studied in §§ 4–6. The disparity between the thickness of the diffusive layer next to the interface and the relevant dimensions of the problem poses a major challenge to the numerical simulation. This challenge can be circumvented by assuming the approximation $\hat{c}_s \sim \hat{c}_\infty$, which leads to accurate results under certain conditions (Lytra *et al.* 2024). As explained in § 3, we resolve the surfactant mass boundary layer by using a spatial discretization based on Chebyshev spectral collocation points (Khorrami 1989).

The effect of the surface concentration $\hat{\Gamma}$ on the surface tension $\hat{\gamma}$ is described by the Langmuir equation of state (Tricot 1997)

$$\hat{\gamma} = \hat{\gamma}_* + \hat{\Gamma}_\infty \hat{R}_g T \ln\left(1 - \frac{\hat{\Gamma}}{\hat{\Gamma}_\infty}\right), \tag{2.3}$$

where $\hat{R}_g$ is the gas constant and T is the temperature. This equation can be derived from (2.2*a–c*) and the Gibbs isotherm (Chang & Franses 1995). The surface tension variation over the interface gives rise to the local soluto-capillarity effect and Marangoni stress.

As mentioned in the Introduction, we do not consider surface rheology effects. The effects of the shear μ_1^S and dilatational μ_2^S surface viscosities can be quantified in terms of the superficial Ohnesorge numbers $Oh_{1,2}^S = \mu_{1,2}^S(\rho_i \hat{\gamma}_c \hat{R}_c^3)^{-1/2}$, which measure the relative importance of the surface viscous stresses and the capillary pressure. Ponce-Torres *et al.* (2020) concluded that the SDS viscosities are at most of the order of 10^{-7} Pa · s · m. Then, the Ohnesorge numbers are at most of the order of 10^{-2} in our problem, which indicates that SDS surface viscosities can be neglected.

2.3. *Dimensionless numbers*

We choose the feeding capillary radius $\hat{R}_c$, the visco-capillary velocity $v_{\gamma\mu} = \hat{\gamma}_c/\mu_i$ and the capillary pressure $\hat{\gamma}_c/\hat{R}_c$ as the characteristic quantities, where $\hat{\gamma}_c$ is a characteristic value of the surface tension, whose choice will be discussed below.

In the absence of surfactants, the problem can be formulated in terms of the density and viscosity ratios, $\rho = \rho_o/\rho_i$ and $\mu = \mu_o/\mu_i$, the Ohnesorge and capillary numbers

$$Oh_i = \left(\frac{\mu_i}{\rho_i v_{\gamma\mu}\hat{R}_c}\right)^{1/2} = \frac{\mu_i}{(\rho_i\hat{\gamma}_c\hat{R}_c)^{1/2}} \quad \text{and} \quad Ca = \frac{\mu_o U}{\hat{\gamma}_c}, \tag{2.4a,b}$$

and the flow rate ratio $Q = Q_i/Q_o$. Here, $U = 4Q_o/(\pi\hat{D}^2)$ is the mean velocity in the nozzle neck. The capillary number is the ratio of the characteristic viscous stress $\mu_o U/\hat{R}_c$ to the capillary pressure $\hat{\gamma}_c/\hat{R}_c$.

When a soluble surfactant is added to the disperse phase, the following dimensionless numbers are considered as well: the bulk and surface Péclet numbers $Pe = \hat{R}_c v_{\gamma\mu}/\hat{\mathcal{D}}_i$ and $Pe_s = \hat{R}_c v_{\gamma\mu}/\hat{\mathcal{D}}_s$, the dimensionless adsorption and desorption constants $k_a = \hat{k}_a\hat{c}_{cmc}\hat{R}_c/(\hat{\Gamma}_\infty v_{\gamma\mu})$ and $k_d = \hat{k}_d\hat{R}_c/v_{\gamma\mu}$, the Marangoni (elasticity) number $Ma = \hat{\Gamma}_\infty R_g T/\hat{\gamma}_c$ and the reservoir surfactant concentration $c_\infty = \hat{c}_\infty/\hat{c}_{cmc}$.

There are two natural choices for the characteristic surface tension: (i) the value $\hat{\gamma}_*$ corresponding to the surfactant-free case and (ii) the equilibrium value $\hat{\gamma}_{eq}$ corresponding to reservoir concentration $\hat{c}_\infty$. As shown in § 4, surfactant molecules are convected downstream by the interface, which results in values of the meniscus surface tension much larger than $\hat{\gamma}_{eq}$. For this reason, we consider $\hat{\gamma}_*$ in the definition of the dimensionless numbers.

For a fixed geometry, the set of dimensionless numbers governing the problem is $\{\rho, \mu, \mathrm{Oh}_i, Ca, Q; Pe, Pe_s, k_a, k_d, Ma, c_\infty\}$. In a typical experimental run, the microfluidic device, the fluids and the surfactant are fixed. For this reason, the variables Ca and Q can be regarded as the control parameters. To determine the stability limit, one selects the outer flow rate Q_o and progressively decreases the inner flow rate Q_i until its minimum value $Q_{i\,min}$ for microjetting is reached. The experiment is usually repeated for several values of Q_o. Therefore, the goal is to determine the dimensionless minimum flow rate $Q_{min} = Q_{i\,min}/Q_o$ as a function of Ca. In the presence of a surfactant, the function $Q_{min} = Q_{min}(Ca)$ must be obtained for different values of c_∞ (see § 7).

3. Governing equations and numerical method

This paper analyses numerically the stability of liquid–liquid flow focusing in a converging nozzle when a surfactant is dissolved in the inner phase. For this purpose, we consider the full hydrodynamic equations, including inertia, without any approximations relative to the surfactant transport. The dimensionless Navier–Stokes equations for the axisymmetric velocity $\boldsymbol{v}^{(k)}(r, z; t)$ and pressure $p^{(k)}(r, z; t)$ fields are

$$(ru^{(k)})_r + rw_z^{(k)} = 0, \tag{3.1}$$

$$\rho^{\delta_{ko}}(Oh_i)^{-2}\left(\frac{\partial u^{(k)}}{\partial t} + u^{(k)}u_r^{(k)} + w^{(k)}u_z^{(k)}\right) = -p_r^{(k)} + \mu^{\delta_{ko}}(u_{rr}^{(k)} + (u^{(k)}/r)_r + u_{zz}^{(k)}), \tag{3.2}$$

$$\rho^{\delta_{ko}}(Oh_i)^{-2}\left(\frac{\partial w^{(k)}}{\partial t}+u^{(k)}w_r^{(k)}+w^{(k)}w_z^{(k)}\right)=-p_z^{(k)}+\mu^{\delta_{ko}}(w_{rr}^{(k)}+w_r^{(k)}/r+w_{zz}^{(k)}), \tag{3.3}$$

where t is the time, r (z) is the radial (axial) coordinate, $u^{(k)}$ ($w^{(k)}$) is the radial (axial) velocity component and δ_{ko} is the Kronecker delta. In the above equations and henceforth, the superscripts $k = i$ and o refer to the inner and outer phases, respectively. In addition, the subscripts r and z denote the partial derivatives with respect to the corresponding coordinates. The action of the gravitational field has been neglected due to the smallness of the fluid configuration.

The velocity field is continuous at the interface, i.e.

$$\boldsymbol{v}^{(i)}=\boldsymbol{v}^{(o)}, \tag{3.4}$$

at $r = F(z, t)$, where $F(z, t)$ is the distance of an interface element to the symmetry axis (figure 2). The kinematic compatibility at the interface yields

$$\frac{\partial F}{\partial t}+F_z w^{(i)}-u^{(i)}=0. \tag{3.5}$$

The equilibrium of normal stresses on that surface leads to

$$-p^{(i)}+\tau_n^{(i)}=\gamma\kappa-p^{(o)}+\tau_n^{(o)}, \tag{3.6}$$

where $\gamma=\hat{\gamma}/\hat{\gamma}_*$ is the normalized surface tension

$$\kappa=\frac{FF_{zz}-1-F_z^2}{F(1+F_z^2)^{3/2}}, \tag{3.7}$$

is the local mean curvature and

$$\tau_n^{(i)}=\frac{2[u_r^{(i)}-F_z(w_r^{(i)}+u_z^{(i)})+F_z^2 w_z^{(i)}]}{1+F_z^2}, \tag{3.8}$$

$$\tau_n^{(o)}=\frac{2\mu[u_r^{(o)}-F_z(w_r^{(o)}+u_z^{(o)})+F_z^2 w_z^{(o)}]}{1+F_z^2}, \tag{3.9}$$

are the inner and outer normal viscous stresses, respectively. The equilibrium of tangential stresses yields

$$\tau_t^{(i)}+\tau^{Ma}=\tau_t^{(o)}, \tag{3.10}$$

where $\tau_t^{(i)}$ is the inner tangential viscous stress, τ^{Ma} is the Marangoni stress and $\tau_t^{(o)}$ is the outer tangential viscous stress given by the expressions

$$\tau_t^{(i)}=(1-F_z^2)(w_r^{(i)}+u_z^{(i)})+2F_z(u_r^{(i)}-w_z^{(i)}), \tag{3.11}$$

$$\tau^{Ma}=-\gamma_z(1+F_z^2)^{1/2}, \tag{3.12}$$

$$\tau_t^{(o)}=\mu[(1-F_z^2)(w_r^{(o)}+u_z^{(o)})+2F_z(u_r^{(o)}-w_z^{(o)})]. \tag{3.13}$$

As mentioned in § 2, the viscous surface stresses have been neglected in (3.6) and (3.10).

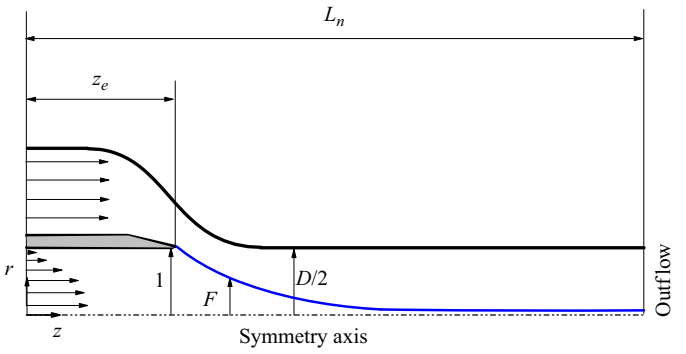

Figure 2. Sketch of the computational domain.

The surfactant volumetric concentration (measured in terms of the critical micelle concentration) $c^{(i)}(\boldsymbol{r}, t)$ is calculated from the conservation equation (Craster, Matar & Papageorgiou 2009; Kalogirou & Blyth 2019)

$$\frac{\partial c^{(i)}}{\partial t} + u^{(i)} c_r^{(i)} + w^{(i)} c_z^{(i)} = Pe^{-1}[(r c_r^{(i)})_r / r + c_{zz}^{(i)}]. \tag{3.14}$$

We assume that monomers are at equilibrium with micelles at concentrations exceeding the critical micelle concentration. Therefore, the net flux of micelle formation/destruction vanishes.

The net sorption flux $\mathcal{J} = \hat{\mathcal{J}} \hat{R}_c / (v_{\gamma\mu} \hat{\Gamma}_\infty)$ at the interface is calculated as (2.2*a–c*) (Craster *et al.* 2009; He *et al.* 2015; Kalogirou & Blyth 2019)

$$\mathcal{J} = \mathcal{J}_a - \mathcal{J}_d, \quad \mathcal{J}_a = k_a c_s^{(i)} (1 - \Gamma), \quad \mathcal{J}_d = k_d \Gamma, \tag{3.15a–c}$$

where $\mathcal{J}_a = \hat{\mathcal{J}}_a \hat{R}_c / (v_{\gamma\mu} \hat{\Gamma}_\infty)$ and $\mathcal{J}_d = \hat{\mathcal{J}}_d \hat{R}_c / (v_{\gamma\mu} \hat{\Gamma}_\infty)$ are the dimensionless adsorption and desorption fluxes, respectively, $c_s^{(i)}$ is the surfactant concentration evaluated at the interface and $\Gamma = \hat{\Gamma} / \hat{\Gamma}_\infty$ is the dimensionless surfactant surface concentration. The net sorption flux equals the surfactant diffused from/to the bulk $\mathcal{J}_{\mathcal{D}}$; i.e.

$$\mathcal{J} = \mathcal{J}_{\mathcal{D}} = \left. \frac{c_z^{(i)} F_z - c_r^{(i)}}{Pe \sqrt{1 + F_z^2}} \right|_{r=F}. \tag{3.16}$$

This equation couples surfactant transport across the bulk and over the interface.

The surfactant surface concentration Γ satisfies the advection–diffusion equation (Craster *et al.* 2009)

$$\frac{\partial \Gamma}{\partial t} + \boldsymbol{\nabla}_s \cdot (\Gamma \boldsymbol{v}_s) + \Gamma \kappa (\boldsymbol{v} \cdot \boldsymbol{n}) = \frac{1}{Pe_s} \boldsymbol{\nabla}_s^2 \Gamma + \mathcal{J}, \tag{3.17}$$

where $\boldsymbol{v}_s = \mathsf{I}_s \boldsymbol{v} = v_s \boldsymbol{t}$ is the (two-dimensional) surface velocity, $\boldsymbol{t}$ is the tangential unit vector, $\mathsf{I}_s = \mathsf{I} - \boldsymbol{nn}$ is the tensor that projects any vector on that surface, I is the identity tensor, $\boldsymbol{n}$ is the unit outward normal vector and $\boldsymbol{\nabla}_s$ is the tangential intrinsic gradient along the free surface parametrized with the intrinsic coordinate s. The above equation can be

re-written as

$$\frac{\partial \Gamma}{\partial t} + \Gamma\left(\frac{\mathrm{d}v_s}{\mathrm{d}s} + \frac{\mathrm{d}F/\mathrm{d}s}{F}v_s\right) + \frac{\mathrm{d}\Gamma}{\mathrm{d}s}v_s + \Gamma\kappa(\boldsymbol{v}\cdot\boldsymbol{n}) = \frac{1}{Pe_s}\left(\frac{\mathrm{d}^2\Gamma}{\mathrm{d}s^2} + \frac{\mathrm{d}\Gamma}{\mathrm{d}s}\,\frac{\mathrm{d}F/\mathrm{d}s}{F}\right) + \mathcal{J}, \tag{3.18}$$

$$v_s = \frac{w^{(i)} + F_z u^{(i)}}{(1+F_z^2)^{1/2}}, \quad \boldsymbol{v}\cdot\boldsymbol{n} = \frac{u^{(i)} - F_z w^{(i)}}{(1+F_z^2)^{1/2}}, \quad \frac{\mathrm{d}A}{\mathrm{d}s} = \frac{A_z}{(1+F_z^2)^{1/2}}, \tag{3.19a–c}$$

where A is any scalar quantity.

The dependence of the surface tension γ upon the surfactant surface concentration Γ is calculated from the Langmuir equation of state (2.3) (Tricot 1997), which in dimensionless form is

$$\gamma = 1 + Ma\log(1-\Gamma). \tag{3.20}$$

The hydrodynamic equations are integrated within the numerical domain sketched in figure 2. We prescribe a parabolic velocity distribution at the inlet section of the feeding capillary, while a uniform velocity profile is imposed at the inlet section of the outer tube. This approximately corresponds to many flow focusing experiments in which a short nozzle is connected to a large tank to drive the outer fluid. Conversely, the inner feeding capillary is usually very long in terms of its diameter.

We consider the no-slip boundary condition at the solid walls and the outflow conditions $u_z^{(k)} = w_z^{(k)} = F_z = 0$ at the right-hand end of the computational domain ($F_z = 0$ only holds at the interface). The anchorage condition of the triple contact line, $F = 1$, is imposed at the edge of the feeding capillary. The reservoir surfactant concentration c_∞ is imposed at the inlet section of the feeding capillary. The numerical integration of (3.17) is performed considering zero surfactant diffusive flux at the triple contact line and the outlet section. We consider the standard regularity conditions $u^{(i)} = w_r^{(i)} = c_r^{(i)} = 0$ at the symmetry axis.

In the global stability analysis, we assume the temporal dependence

$$\left.\begin{aligned} U(r,z;t) &= U_0(r,z) + \delta U(r,z)\,\mathrm{e}^{-\mathrm{i}\omega t} + \text{c.c.} \quad (|\delta U| \ll U_0),\\ F(z;t) &= F_0(z) + \delta F(z)\,\mathrm{e}^{-\mathrm{i}\omega t} + \text{c.c.} \quad (|\delta F| \ll F_0),\\ \Gamma(z;t) &= \Gamma_0(z) + \delta\Gamma(z)\,\mathrm{e}^{-\mathrm{i}\omega t} + \text{c.c.} \quad (|\delta\Gamma| \ll \Gamma_0), \end{aligned}\right\} \tag{3.21}$$

where $U(r,z;t)$ represents the velocity, pressure and bulk surfactant concentration fields, while $U_0(r,z)$ and $\delta U(r,z)$ stand for the base flow (steady) solution and the spatial dependence of the eigenmode, respectively. In addition, $F_0(z)$ and $\Gamma_0(z)$ represent the base flow solution for $F(z)$ and $\Gamma(z)$, respectively, while δF and $\delta\Gamma$ are the corresponding perturbation amplitudes. The perturbation evolves according to the eigenfrequency $\omega = \omega_r + \mathrm{i}\omega_i$, where ω_r and ω_i are the oscillation frequency and growth rate, respectively. The flow asymptotic linear stability (Theofilis 2011) is determined by the eigenfrequency $\omega^* = \omega_r^* + \mathrm{i}\omega_i^*$ of the dominant mode (that with the largest growth rate). Microjetting realizations with $\omega_i^* < 0$, $\omega_i^* = 0$ and $\omega_i^* > 0$ correspond to stable, marginally stable and unstable flows, respectively.

As observed in (3.21), we restrict ourselves to axisymmetric perturbations, which are known to be dominant in experiments. In fact, non-axisymmetric instability appears only for sufficiently large aerodynamic Weber numbers $\mathrm{We} = \rho_o(U-v_j)^2 d_j/\hat{\gamma}_c$ defined in terms of the mean jet and outer stream velocities, v_j and U, and the jet diameter d_j. This instability cannot occur in our configuration. The low value of the Reynolds number

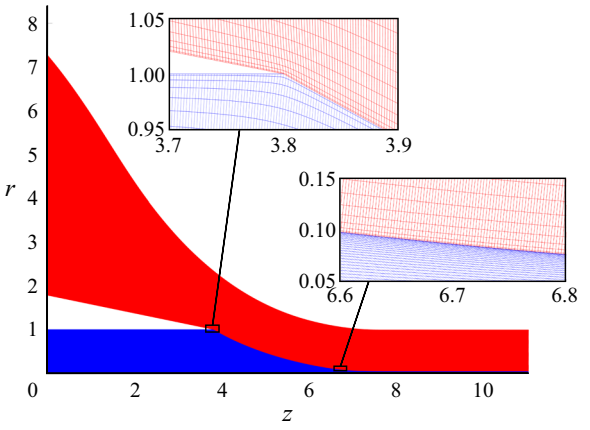

Figure 3. Detail of the grid used in the simulations.

ensures that the flow adopts the Poiseuille solution practically at the entrance of the discharge tube (figure 7), and the aerodynamic Weber number equals 0.054.

The governing equations are integrated with a variant of the numerical method proposed by Herrada & Montanero (2016) and Herrada (2023). This method, as applied to liquid–liquid flow focusing without surfactant, was explained in detail by Cabezas *et al.* (2021). As mentioned in § 2, the major difficulty associated with a soluble surfactant is the existence of a very thin diffusive boundary layer next to the interface for the small diffusion coefficients of most surfactants. However, using Chebyshev spectral collocation points to discretize the radial direction accumulates the grid points next to the interface (Herrada & Montanero 2016), facilitating the resolution of this layer (figure 3).

The inner and outer fluid domains were mapped onto two quadrangular domains through a non-singular mapping. The shape functions were obtained as a part of the solution by using a quasi-elliptic transformation (Dimakopoulos & Tsamopoulos 2003). Some additional boundary conditions for the shape functions were needed to close the problem. All the derivatives appearing in the governing equations were expressed in terms of the spatial coordinates (χ, ξ) resulting from the mapping. These equations were discretized in the (mapped) radial direction with $n_\chi^i = n_\chi^o = 50$ Chebyshev spectral collocation points (Khorrami 1989) in the inner and outer domains. We used fourth-order finite differences with $n_\xi^{(i)} = n_\xi^{(o)} = 4501$ equally spaced points to discretize the (mapped) axial direction in the inner and outer phases.

The Matlab EIGS function was applied to find the eigenfrequencies around a reference value $\tilde{\omega}$. This process was repeated for several values of $\tilde{\omega}$ to obtain part of the eigenfrequency spectrum. We conducted a grid sensitivity analysis to ensure the grid size did not affect the results. We verified that the surfactant surface density, interface velocity and critical eigenfrequency differed by less than 1 % when the number of grid points was increased by 50 %.

We also conducted transient (direct) numerical simulations to show the response of the microjetting mode to an initial perturbation. The numerical method is essentially the same as that used in the stability analysis. We used the spatial discretization of the mapped numerical domain described above. The time domain was discretized with second-order backward finite differences. The time step $\Delta t = 0.5$ was constant. We verified that reducing the time step did not significantly change the results.

The rest of this paper is organized as follows. Section 4 describes the base flow for a reference case characterized by realistic values of the governing parameters. Section 5 analyses the stabilizing effect of the surfactant monolayer in that case by comparing the results with and without surfactant. Section 6 shows transient numerical simulations in the presence of the surfactant for the reference case too. § 7 explores the system's response when the surfactant parameters are changed. Finally, concluding remarks are presented in § 8.

4. Base flow of the reference case

As the reference case, we consider the configuration characterized by the following realistic parameters. The nozzle shape and the feeding capillary position are the same as those in the experiments of Cabezas *et al.* (2021). The capillary radius is $\hat{R}_c = 0.1$ mm. In terms of this characteristic length, the relevant lengths in the simulations are $L_n = 11.4$, $z_e = 3.8$ and $D = 2$ (figure 2). We consider the physical properties very similar to those of the water–oil system studied by Moyle *et al.* (2012): $\rho_i = 998$ kg m^{-3}, $\rho_o = 830$ kg m^{-3}, $\mu_i = 1.33$ mPa·s, $\mu_o = 53.1$ mPa·s and $\hat{\gamma}_* = 62$ mN m^{-1}. We consider the surfactant properties reported by Liang *et al.* (2022) for SDS in a water–nOctane system: $\hat{\mathcal{D}}_i = 7.9 \times 10^{-10}$ m^2 s^{-1}, $\hat{\mathcal{D}}_s = 7.9 \times 10^{-10}$ m^2 s^{-1}, $\hat{\Gamma}_\infty = 3.13$ μmol m^{-2}, $R_g = 8.314$ J (K mol)$^{-1}$, $\hat{k}_a = 8.25 \times 10^{-5}$ m s^{-1}, $\hat{k}_d = 1.3$ s^{-1} and $\hat{c}_{cmc} = 8.3$ mol m^{-3}. The corresponding values of the dimensionless numbers are $\rho = 0.83$, $\mu = 40$, $Oh_i = 0.0169$, $Pe = 5.89 \times 10^6$, $Pe_s = 5.89 \times 10^6$, $k_a = 4.71 \times 10^{-4}$, $k_d = 2.79 \times 10^{-6}$ and $Ma = 0.117$. All the results were calculated for these values unless otherwise specified.

The condition $c_\infty > 1$ (a concentration larger than the critical micelle concentration) is necessary to observe a significant surfactant effect in the experiments (Moyle *et al.* 2012; López *et al.* 2022). For this reason, we consider the surfactant concentration $c_\infty = 1.47$. As explained below, this concentration is sufficiently small for the Langmuir equation to provide reliable interfacial tension values. We select the capillary number $Ca = 0.349$, a similar value to those of the experiments of Cabezas *et al.* (2021).

The results presented in this section correspond to the marginally stable ($\omega_i = 0$) case obtained for $Q = 0.005$. These results are compared with those of the unstable ($\omega_i > 0$) base flow without surfactant obtained for the same values of the governing parameters.

Figure 4 shows the surfactant volumetric concentration for the reference case. Due to the small value of the diffusion coefficient, a thin mass boundary layer separates the stream coming from the feeding capillary from the recirculating cells that occupy the tapering meniscus. The surfactant is convected across a narrow annular streamtube next to the interface. The surfactant molecules adsorb onto the interface according to the kinetic model (3.15*a–c*). Adsorption occurs mostly next to the feeding capillary (figure 5), where the adsorption flux is higher (the interface is empty), the interface area is larger and the surface velocity is smaller.

The liquid flowing next to the interface is slightly emptied of surfactant downstream. Flow recirculation convects this small surfactant depletion throughout the tapering meniscus (figure 4). Overall, the surfactant volumetric concentration is relatively constant in the fluid domain ($1.33 \leq c^{(i)} \leq 1.47$), including the sublayer next to the interface. This behaviour was also described by Lytra *et al.* (2024) for a similar configuration.

As mentioned above, the volumetric surfactant concentration evaluated at the free surface, $c_{0s}^{(i)}$, practically takes the upstream value c_∞. This can be anticipated from a simple

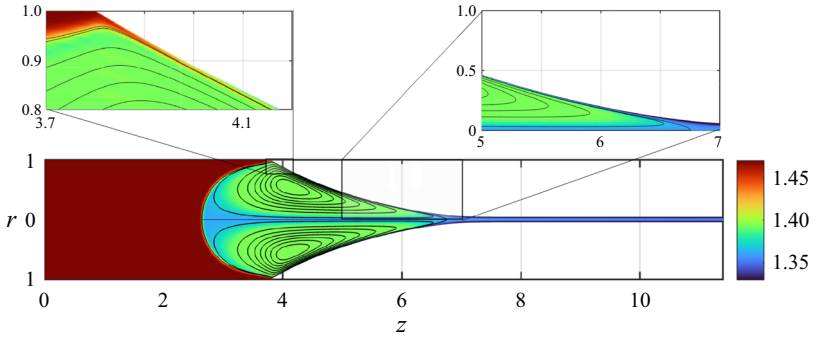

Figure 4. Surfactant volumetric concentration $c_0^{(i)}(r.z)$ for $Ca = 0.349$, $Q = 0.005$ and $c_\infty = 1.47$. The lines are the streamlines.

scaling analysis. Consider the surfactant boundary layer next to the interface. According to (3.15*a–c*), the variation $\Delta c_0^{(i)}$ of surfactant concentration across that layer can be estimated as

$$\widetilde{Pe}^{-1}\frac{\Delta c_0^{(i)}}{\lambda_D} \sim \frac{\tilde{k}_a}{v_\lambda} c_{0s}^{(i)}, \tag{4.1}$$

where $\widetilde{Pe} = \hat{v}_\lambda \hat{R}_c/\hat{\mathcal{D}}_i$ is the Péclet number defined in terms of the characteristic velocity $\hat{v}_\lambda$ in the surfactant boundary layer, $\lambda_D \sim \widetilde{Pe}^{-1/2}$ is the (dimensionless) boundary layer thickness (Levich 1962), $\tilde{k}_a = \hat{k}_a/v_{\gamma\mu}$ and $v_\lambda = \hat{v}_\lambda/v_{\gamma\mu}$. The order of magnitude of the ratio $\Delta c_0^{(i)}/c_{0s}^{(i)}$ is

$$\frac{\Delta c_0^{(i)}}{c_{0s}^{(i)}} \sim \frac{\tilde{k}_a}{v_\lambda}\widetilde{Pe}^{1/2}. \tag{4.2}$$

The Schmidt number $\mathrm{Sc} = \mu_i/\rho_i\hat{\mathcal{D}}_i$ is of the order of 10^3, which implies that λ_D is much smaller than the characteristic viscous diffusion length. For this reason, we can assume that $v_\lambda \sim v_0^s \sim 10^{-2}$ (figure 5). This implies that $\widetilde{Pe} \sim 10^5$, $\lambda_D \sim 10^{-3}$–10^{-2} and $\Delta c^{(i)}/c_{0s}^{(i)} \sim 10^{-2}$–$10^{-1}$, which is consistent with the numerical results. We conclude that convection ensures $c_{0s}^{(i)} \simeq c_\infty$ throughout the inner fluid domain. This constitutes an advantage numerically because it makes discretization errors in the boundary layer less relevant.

As mentioned above, adsorption occurs mostly next to the feeding capillary. However, a sharp reduction of the interface radius occurs in the meniscus tip. The reduction of the interface area considerably increases the surfactant surface concentration there (figure 5). The increase in the surfactant surface concentration leads to a significant decrease in the surface tension (figure 5).

The residence time of the interface element in the meniscus tip takes relatively small values due to the higher surface velocities there. This effect hinders surfactant desorption, which is almost negligible throughout the interface (figure 5) even though the surfactant surface density approaches the maximum packing density in the meniscus tip (figure 5).

The surfactant concentration $c_\infty = 1.47$ leads to the surface coverage $\Gamma_{eq} = 0.997$ at equilibrium, which would render the Langmuir model inaccurate. However, the surfactant molecules are convected downstream in the present dynamical problem, which significantly reduces the surface coverage and allows one to use the Langmuir equation of state safely even for concentrations higher than the critical micelle concentration.

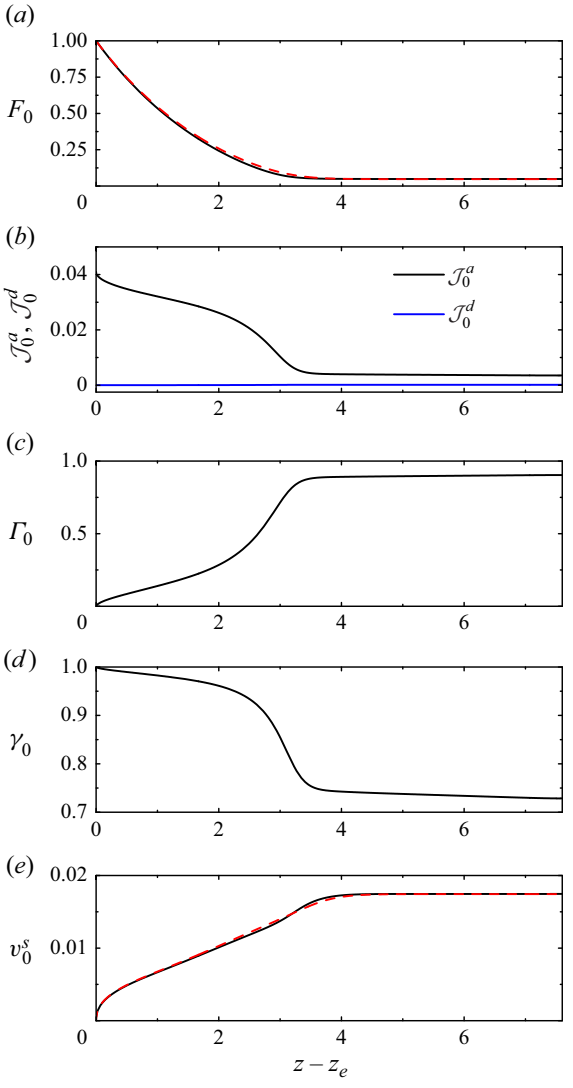

Figure 5. Interface location $F_0(z)$ (*a*), adsorption flux $\mathcal{J}_0^a(z)$, desorption flux $\mathcal{J}_0^d(z)$ (*b*), surface concentration $\Gamma_0(z)$ (*c*), surface tension $\gamma_0(z)$ (*d*) and surface velocity $v_0^s(z)$ (*e*) for $Ca = 0.349$, $Q = 0.005$, and $c_\infty = 1.47$. The red dashed lines indicate the interface location and velocity without surfactant. Here, z_e is the axial coordinate of the capillary exit.

In fact, $c_\infty = 1.47$ leads to surface tension reduction in our simulation smaller than 30 % (figure 5), much smaller than that at equilibrium for the same concentration (Liang *et al.* 2022).

The Marangoni stress in the meniscus tip acts against the viscous drag exerted by the outer flow. This substantially alters the balance of the tangential stresses at the interface. Specifically, the viscous drag exerted by the outer stream increases in the presence of surfactant (figure 6). However, the momentum transfer to the inner phase is slightly smaller. As explained in § 5, the decrease in the inner-phase flow rate dragged by the outer current stabilizes the flow. The increase in the viscous drag exerted by the external stream entails an increase in the pressure drop driving the outer phase.

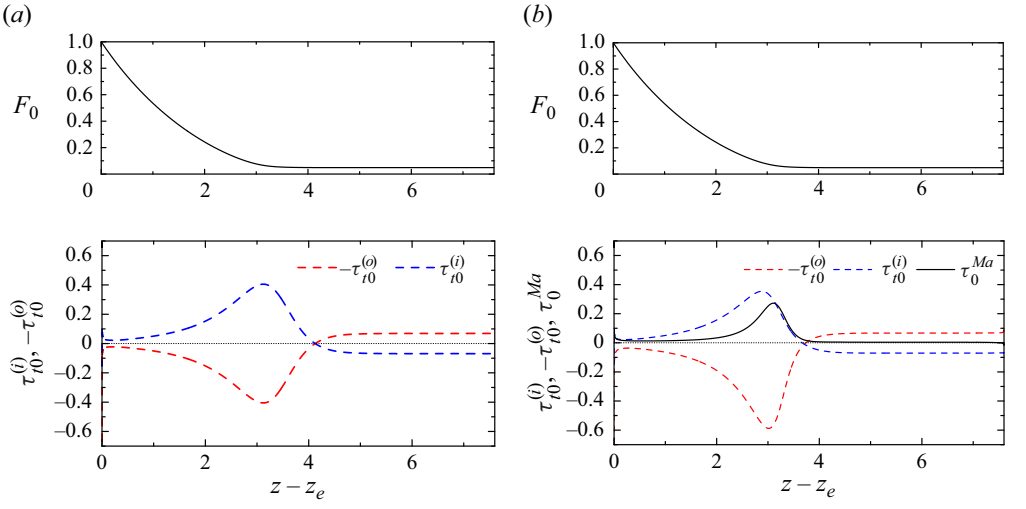

Figure 6. Interface location $F_0(z)$ and tangential stress at the interface: outer viscous stress $\tau_{t0}^{(o)}$, inner viscous stress $\tau_{t0}^{(i)}$ and Marangoni stress τ_0^{Ma}. The results were calculated for $Ca = 0.349$, $Q = 0.005$ and $c_\infty = 0$ (a) and 1.47 (b).

The surface velocity v_s is of the order of the mean velocity in the nozzle neck, which implies that $v_s \sim Ca/\mu \sim 10^{-2}$, as shown below. Interestingly, the Marangoni stress magnitude is insufficient to reduce the surface velocity. Figures 5 and 6 show that Marangoni stress tries to immobilize the interface in the meniscus tip, where the surface tension gradient takes higher values. However, the flow practically develops at the entrance of the nozzle neck due to the large viscosity forces (figure 7). The value of v_s downstream is fixed by the Hagen–Poiseuille parabolic profiles, which are unaffected by the surfactant. Therefore, $v_s(z)$ takes practically the same value with and without surfactant. This behaviour substantially differs from that observed in open flows, where the Marangoni stress reduces the interface velocity and, therefore, the intensity of the inner flow (Frumkin & Levich 1947; Herrada *et al.* 2022).

The jet radius R_j, the pressure gradient K and the interface velocity v_s in the discharge tube are approximately given by the fully developed flow formulae

$$R_j = \left(\frac{Q}{1 + Q + \sqrt{1 + Q\mu}}\right)^{1/2}, \tag{4.3}$$

$$K = -8Ca\mu^{-2}[2 + \mu(Q + \mu - 2) + 2(\mu - 1)\sqrt{1 + Q\mu}], \tag{4.4}$$

and

$$v_s = 2Ca\mu^{-2}(\mu - 1 + \sqrt{1 + Q\mu}). \tag{4.5}$$

The values of R_j and v_s evaluated at the outlet of the numerical domain are 0.04859 and 0.01747, respectively, while the corresponding analytical predictions (4.3)–(4.5) are 0.04879 and 0.01749. Equation (4.3) shows that the jet diameter d_j scales as $Q_i^{1/2}$ for $Q \ll 1$ and $Q\mu \ll 1$. It is worth mentioning that the condition $Q\mu \ll 1$ does not verify in our simulations even though $Q \ll 1$. For instance, $Q\mu = 0.2$ and 0.5 at the stability limit with and without surfactant, respectively.

As mentioned above, the surfactant accumulates in the meniscus tip interface. The surfactant effect is localized in that region. For this reason, the base flows with and

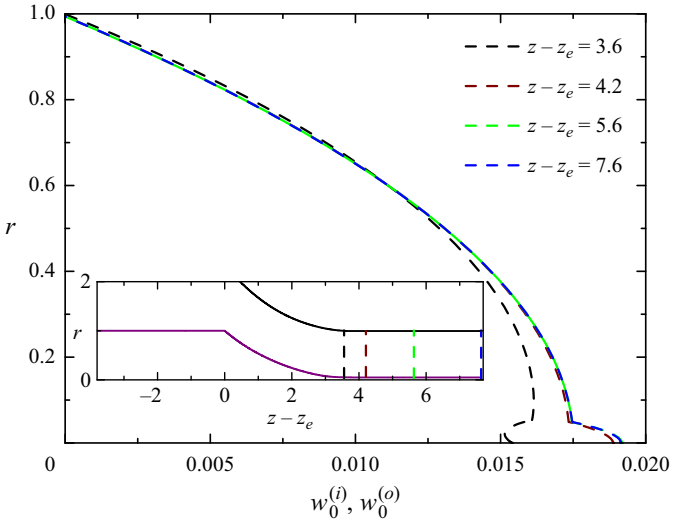

Figure 7. Axial velocity profile, $w_0^{(i)}$ and $w_0^{(o)}$, at the nozzle sections $z - z_e = 3.6$, 4.2, 5.6 and 7.6. The results were calculated for $Ca = 0.349$, $Q = 0.005$ and $c_\infty = 1.47$. The inset shows the nozzle sections corresponding to the velocity profiles.

without surfactant are similar on the scale given by the feeding capillary radius (figure 8). In particular, the surfactant monolayer does not significantly alter the interface location $F_0(z)$. The surfactant slightly reduces the recirculation cell size, making the stagnation point in the meniscus tip move upstream (figure 9). However, the surfactant hardly affects the upstream stagnation point location. This indicates that the stabilization caused by the surfactant (see § 5) is not related to the penetration of the recirculation cell into the feeding capillary, a destabilizing mechanism in gaseous flow focusing (Montanero & Gañán-Calvo 2020).

As explained in § 5, the instability originates in the meniscus–jet transition region. The decrease in capillary pressure caused by the surfactant monolayer in that region considerably reduces the pressure force opposing the flow (figure 9). This partially explains why the surfactant stabilizes the flow. We will return to this in § 5.

5. Linear stability analysis of the reference case

This section analyses the linear stability of the reference case considered in the previous section. We explain how the surfactant monolayer stabilizes the flow by studying its effect on the perturbations and the base flow separately.

As explained in § 2, the set of dimensionless parameters characterizing the present problem are

$$\{\rho, \mu, Oh_i, Ca, Q; Pe, Pe_s, k_a, k_d, Ma, c_\infty\}. \tag{5.1}$$

The subset

$$\{\mathcal{P}_i\} \equiv \{Pe, Pe_s, k_a, k_d, Ma, c_\infty\}, \tag{5.2}$$

accounts for the surfactant effect. The linearized equations governing the perturbations depend on both $\{\mathcal{P}_i\}$ and the base flow Φ_0 around which those equations are linearized. As shown in § 5, the surfactant monolayer affects the base flow Φ_0. This means that the perturbations $\delta\Phi$ depend on $\{\mathcal{P}_i\}$ through (i) the dependence of the linearized equations on $\{\mathcal{P}_i\}$ and (ii) the dependence of the base flow Φ_0 on those parameters. In this sense,

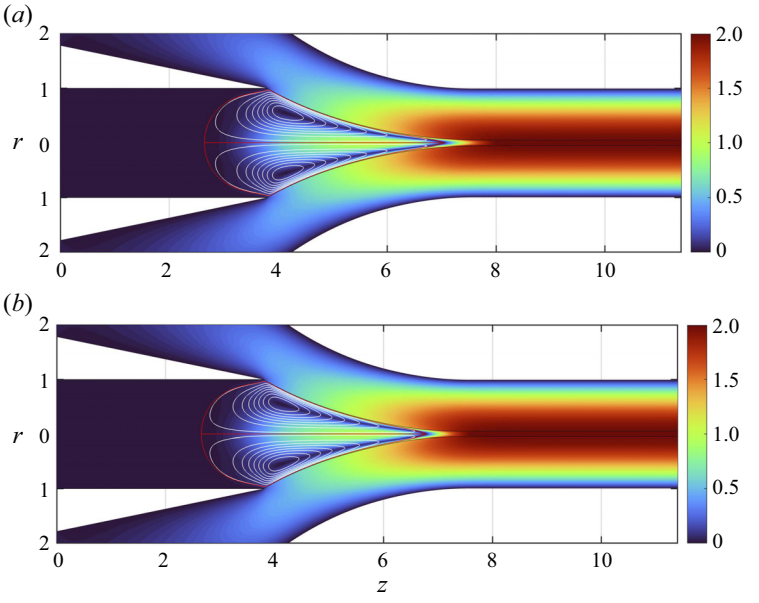

Figure 8. Streamlines for $Ca = 0.349$, $Q = 0.005$ and $c_\infty = 0$ (*a*) and 1.47 (*b*). The colour indicates the velocity magnitude in terms of the mean velocity in the discharge tube U.

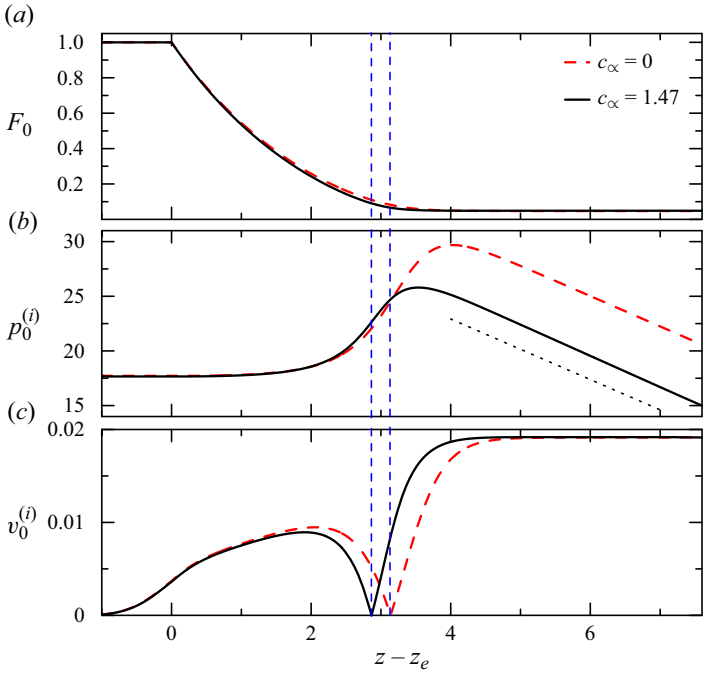

Figure 9. Interface location $F_0(z)$, (*a*) hydrostatic pressure $p_0^{(i)}$ (*b*) and velocity $v_0^{(i)}$ (*c*) at the symmetry axis. The results were calculated for $Ca = 0.349$, $Q = 0.005$ and $c_\infty = 0$ and 1.47. The dashed vertical lines indicate the position of the stagnation points. The dotted line indicates the pressure drop (4.4) corresponding to fully developed flow with constant surface tension.

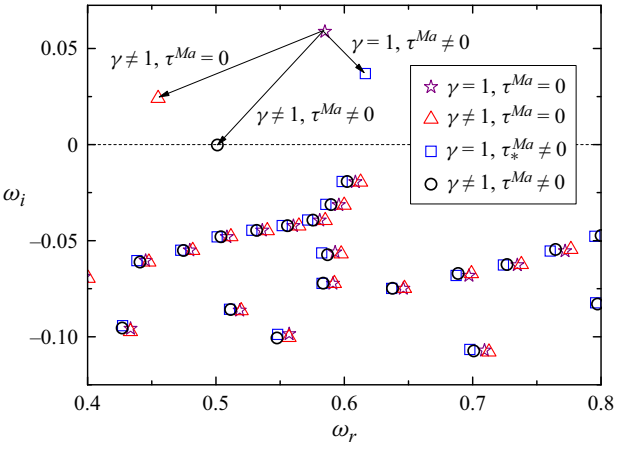

Figure 10. Spectrum of eigenvalues around $\tilde{\omega} = 0.6$ for $Ca = 0.349$ and $Q = 0.005$. The stars are the results when neither soluto-capillarity nor Marangoni stress is considered. The triangles are the results obtained only considering soluto-capillarity. The squares are the results obtained only considering Marangoni stress. The circles correspond to the results when the two effects are considered. The arrows indicate the displacement of the critical mode eigenvalue due to soluto-capillarity and Marangoni stress. The values of Ca and Q approximately correspond to marginal stability ($max\{\omega_i\} = 0$) in the presence of surfactant. The eigenvalues have been made dimensionless with the inertio-capillary time $t_{ic} = (\rho_i \hat{R}_c^3/\gamma_*)^{1/2}$.

$\delta\Phi$ obeys the formal relationship $\delta\Phi = \mathcal{F}(\{\mathcal{P}_i\}, \Phi_0(\{\mathcal{P}_i\}))$. We start our analysis by considering in § 5.1 the combined influence of these two factors. Section 5.2 examines the effect of the surfactant on the perturbations exclusively (for a given base flow). Finally, we discuss the secondary role of the base flow in § 5.3.

5.1. *Surfactant effect on the perturbations and base flow*

The surfactant influence on the system stability through both the perturbations and the base flow can be studied by comparing the results with and without surfactant. In other words, we compare the solutions for $c_\infty = 0$ and $c_\infty = 1.47$. Figure 10 shows the spectrum of eigenvalues in these two cases. The values for $\gamma = 1$ (without soluto-capillarity) and $\tau^{Ma} = 0$ (without Marangoni stress) correspond to $c_\infty = 0$, while the values for $\gamma \neq 1$ and $\tau^{Ma} \neq 0$ correspond to $c_\infty = 1.47$. The addition of surfactant stabilizes the microjetting mode of flow focusing, significantly reducing the critical growth rate. The eigenfrequencies of the subdominant modes are hardly affected by the surfactant monolayer. This means that the major effect of the surfactant monolayer on the system's linear dynamics occurs precisely through the critical eigenmode. This effect significantly affects the stability limit. The minimum flow rate ratio in the absence of surfactant $Q_{min} = 0.0125$ decreases to 0.005 when the surfactant is added.

A supercritical oscillatory Hopf bifurcation ($\omega_r^* \neq 0$) causes the flow instability, as in most tip streaming configurations (Montanero & Gañán-Calvo 2020). The presence of the surfactant monolayer does not alter this result. The critical perturbation oscillation is linked to the presence of the jet. The jet convects capillary modes, translating into an oscillatory behaviour in the Eulerian frame of reference. As in other tip streaming configurations, ω_r^* is commensurate with the inverse of the inertio-capillary time based on the meniscus size.

The importance of soluto-capillarity and Marangoni stress has been assessed separately by 'turning off' the corresponding terms in the interface boundary conditions (3.6) and

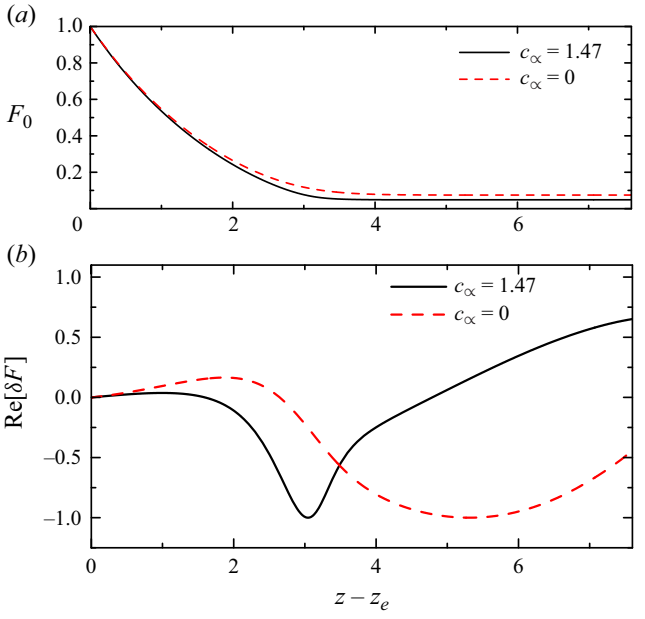

Figure 11. Interface location $F_0(z)$ (*a*) and perturbation of the interface location, $\delta F(z)$, (*b*) for $Ca = 0.349$ and $c_\infty = 0$ and 1.47. The results correspond to the minimum flow rate ratios $Q = 0.0125$ and 0.005 corresponding to $c_\infty = 0$ and 1.47, respectively. The values of Re$[\delta F]$ are normalized by dividing them by the absolute values of the corresponding minimum values.

(3.10). When both soluto-capillarity ($\gamma \neq 1$) and Marangoni stress ($\tau^{Ma} \neq 0$) are present, Q_{min} decreases from 0.0125 to 0.005. If the dependence $\gamma(\Gamma)$ is retained in (3.6) but the term τ^{Ma} is set to 0 in (3.10), Q_{min} decreases from 0.0125 to 0.0075. This means that the two factors significantly contribute to the microjetting stabilization. As expected, there is a correspondence between the magnitude of the decrease in the minimum flow rate due to those factors and the corresponding decrease in the critical growth rate (figure 10): the larger the decrease in Q_{min} associated with either soluto-capillarity or Marangoni stress, the larger the corresponding decrease in ω_i^*.

The surfactant monolayer not only affects the minimum flow rate ratio but also influences the shape of the interface deformation caused by the critical eigenmode. Figure 11 compares $\delta F(z)$ for $c_\infty = 0$ and 1.47 at the corresponding stability limit. The jet diameter is larger without surfactant because the flow rate ratio is larger in that case. The surfactant monolayer increases the interface deformation in the meniscus–jet transition region. This deformation expands upstream and downstream in the absence of surfactant.

5.2. *Surfactant effect on the perturbations*

In the previous section, we analysed the influence of the surfactant on the microjetting stability through its effect on both the perturbations and the base flow. Now, we exclusively examine the surfactant effect on the perturbations, i.e. for a given base flow. Specifically, we consider the marginally stable base flow for $c_\infty = 1.47$ and study the perturbations around this base flow with and without the surfactant effect only on the perturbations (not on the base flow).

In the presence of a surfactant monolayer, the perturbation produces a variation $\delta\gamma(z)\,\mathrm{e}^{-\mathrm{i}\omega t} + \text{c.c.}$ of the surface tension with respect to its value $\gamma_0(z)$ in the base flow.

This variation is the distinct feature of the perturbations suffered by a surfactant-loaded interface. For this reason, we analyse its effect on the spectrum of eigenfrequencies. The amplitude $\delta\gamma$ can be calculated from the linearization of (3.20) as $\delta\gamma = -Ma\delta\Gamma$.

The linearized equation for the balance of normal stresses at the interface reads

$$-\delta p^{(i)} + \delta\tau_n^{(i)} = \gamma_0\delta\kappa + \delta p_\gamma - \delta p^{(o)} + \delta\tau_n^{(o)}, \tag{5.3}$$

where $\delta p^{(i)}$, $\delta p^{(o)}$, $\delta\tau_n^{(i)}$ and $\delta\tau_n^{(o)}$ are the perturbations of the hydrostatic pressure and normal viscous stresses, $\gamma_0(z)$ is the surface tension in the base flow and

$$\delta\kappa = \frac{1}{F_0^2\sqrt{1+F_{0z}^2}}\delta F + \frac{F_0F_{0z} + F_0F_{0z}^3 - 3F_0^2F_{0z}F_{0zz}}{F_02(1+F_{0z}^2)^{5/2}}\delta F_z + \frac{F_0^2 + F_0^2F_{0z}^2}{F_0^2(1+F_{0z}^2)^{5/2}}\delta F_{zz}, \tag{5.4}$$

is the curvature perturbation. The surface tension perturbation $\delta\gamma$ enters into (5.3) through the capillary pressure perturbation $\delta p_\gamma = \delta\gamma\kappa_0$, where κ_0 is the curvature (3.7) in the base flow.

The linearized equation for the balance of tangential stresses is

$$\delta\tau_t^{(i)} + \delta\tau^{Ma} = \delta\tau_t^{(o)}, \tag{5.5}$$

where $\delta\tau_t^{(i)}$ and $\delta\tau_t^{(o)}$ are the perturbations of the tangential viscous stresses, and

$$\delta\tau^{Ma} = \delta\tau_*^{Ma} - \delta F_z\frac{\gamma_{0z}F_{0z}}{\sqrt{1+F_{0z}^2}}, \tag{5.6}$$

is the Marangoni stress perturbation. The surface tension perturbation $\delta\gamma$ enters into (5.6) through the contribution $\delta\tau_*^{Ma} = -\delta\gamma_z(1+F_{0z}^2)^{1/2}$ to the Marangoni stress perturbation.

As mentioned above, the presence of a surfactant monolayer affects the perturbations (excluding the effect on the base flow) through the terms δp_γ and $\delta\tau_*^{Ma}$ in (5.3) and (5.6), respectively. These terms are proportional to surface tension perturbation $\delta\gamma$, which is the distinct characteristic of a surfactant-covered interface. We analyse the influence of these terms on the microjetting stability in figure 12.

Firstly, we consider the eigenfrequencies calculated by setting $\delta\tau_*^{Ma} = 0$ to assess the effect of δp_γ. As observed, this term hardly alters the eigenfrequencies of the subdominant modes and slightly reduces the growth rate of the critical perturbation. Secondly, we consider the eigenfrequencies for $\delta p_\gamma = 0$ to determine the effect of $\delta\tau_*^{Ma}$. The term $\delta\tau_*^{Ma}$ hardly alters the eigenfrequencies of the subdominant perturbations but considerably decreases the growth rate of the critical eigenmode. Lastly, figure 12 also shows the combined effect of these two terms, which leads to the marginal stability of the base flow.

The decrease in ω_i^* for $\delta\tau_*^{Ma} \neq 0$ and $\delta p_\gamma \neq 0$ (figure 12) is similar to that produced for $\gamma \neq 1$ and $\tau^{Ma} \neq 0$ (figure 10), i.e. when the surfactant effect on both the perturbations and the base flow is considered. This suggests that the change in the base flow alone caused by the surfactant plays a secondary role. The main conclusion of the analysis of figure 12 is that the Marangoni stress $\delta\tau_*^{Ma}$ caused by the surface tension perturbation $\delta\gamma$ is the major stabilizing mechanism in the perturbations.

The results in the Appendix show how the capillary pressure perturbation δp_γ and the Marangoni stress perturbation $\delta\tau_*^{Ma}$ drive the inner liquid from one of the sides of the perturbation neck towards the neck. This is a stabilizing effect because it opposes the neck thinning.

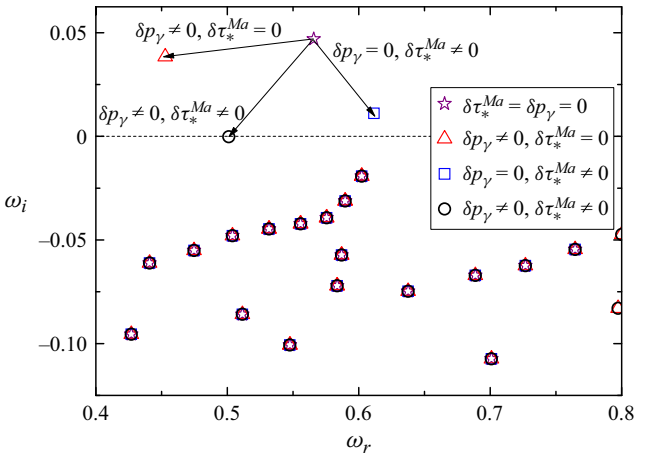

Figure 12. Spectrum of eigenvalues around $\tilde{\omega} = 0.6$ for $Ca = 0.349$ and $Q = 0.005$. The stars are the results when neither of the terms proportional to $\delta\gamma$ is considered. The triangles are the results obtained only considering δp_γ. The squares are the results obtained only considering $\delta\tau_*^{Ma}$. The circles correspond to the results when the two terms are considered. The eigenvalues have been made dimensionless with the inertio-capillary time $t_{ic} = (\rho_i \hat{R}_c^3/\gamma_*)^{1/2}$.

5.3. *Effect of the surfactant on the base flow*

We close our stability analysis by studying the influence of the surfactant on the microjetting stability through its effect only on the base flow. To this end, we compare the eigenfrequencies obtained in the absence of surfactant ($c_\infty = 0$) with those calculated for $c_\infty = 1.47$ but $\delta p_\gamma = \delta\tau_*^{Ma} = 0$. The latter corresponds to the base flow with surfactant but without the surfactant effect on the perturbation.

Figure 13 shows that the surfactant monolayer slightly decreases the frequencies of the subdominant perturbations. The growth (damping) rates remain practically constant. This effect is almost the same as that observed when the surfactant influence on the perturbations and the base flow was considered (figure 10), which confirms that subdominant eigenmodes are only affected through the change of the base flow. The critical mode growth rate decreases when the base flow for $c_\infty = 1.47$ is considered. However, this decrease is much smaller than that produced by the Marangoni stress $\delta\tau_*^{Ma}$ associated with the perturbed surface tension $\delta\gamma$ (figure 12).

The results presented in § 4 allow us to discuss the relatively minor role played by the base flow in the minimum flow rate instability. This instability can be explained in terms of mass conservation. Suppose all the parameters characterizing the problem are fixed except for the flow rate ratio Q (i.e. the inner flow rate Q_i). For sufficiently small values of this parameter, the flow rate dragged by the outer viscous stream becomes practically independent of Q. The dragged flow rate must be replaced through the feeding capillary. This sets a minimum value of Q (Q_i) below which the steady microjetting regime cannot be sustained. The Marangoni stress collaborates with inner viscous stress to balance the outer viscous stress at the interface (figure 11), reducing the dragged flow rate. This allows one to reduce the value of Q (Q_i) while preserving mass conservation.

The stabilizing effect of the surfactant through the base flow can also be explained as follows. As shown in figure 11, the instability originates in the meniscus–jet transition region. The fluid particles experience an adverse pressure gradient ($dp_{\gamma 0}/ds > 0$) when moving next to the interface due to the increase in the capillary pressure $p_{\gamma 0} = \gamma_0 \kappa_0$

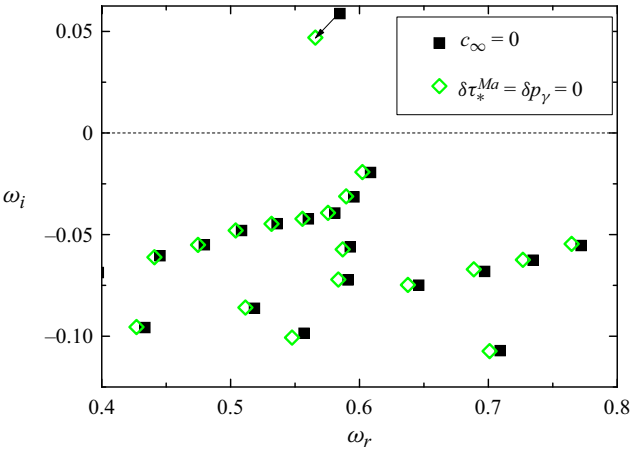

Figure 13. Spectrum of eigenvalues around $\tilde{\omega} = 0.6$ for $Ca = 0.349$ and $Q = 0.005$. The squares are the results without surfactant. The diamonds are the results for $\delta p_\gamma = \delta\tau_*^{Ma} = 0$ (with surfactant but without its effect on the perturbation). The eigenvalues have been made dimensionless with the inertio-capillary time $t_{ic} = (\rho_i \hat{R}_c^3/\gamma_*)^{1/2}$.

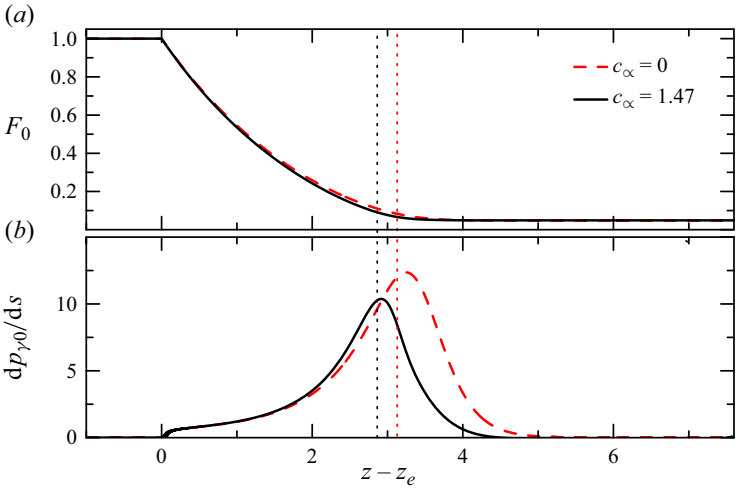

Figure 14. Interface location $F_0(z)$ and surface gradient of the capillary pressure $\mathrm{d}p_{\gamma 0}/\mathrm{d}s$ along the interface. The results were calculated for $Ca = 0.349$, $Q = 0.005$ and $c_\infty = 0$ and 1.47. The dotted vertical lines indicate the position at the symmetry axis of the stagnation points.

downstream (s is the interface intrinsic coordinate) (figure 14). The resulting force opposing the flow in the meniscus tip constitutes another destabilizing mechanism. The surfactant monolayer considerably reduces the capillary pressure in that region (figure 9) and, consequently, the adverse pressure gradient (figure 14). This effect stabilizes the flow.

6. Transient simulations close to the stability limit

This subsection analyses the temporal evolution of a small amplitude perturbation introduced into the base flow close to that of the reference case. We deformed the free surface (the velocity and pressure fields were not perturbed) at $t = 0$. The deformation

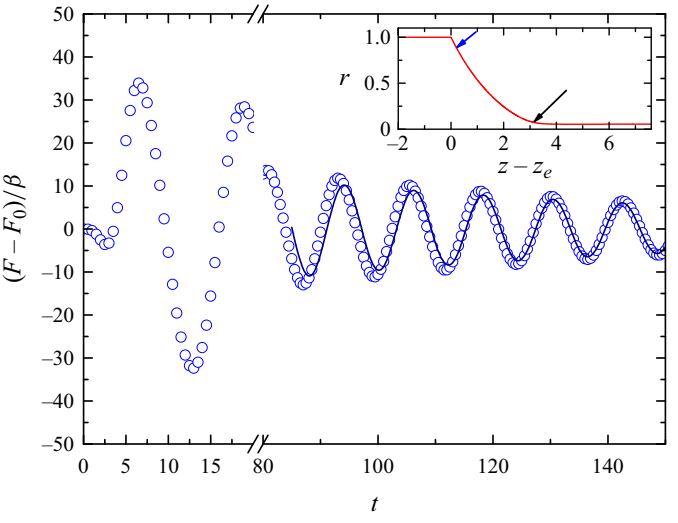

Figure 15. Evolution of the free surface displacement, $F(z, t) - F_0(z)$, at the meniscus tip ($z - z_e = 3.2$, $F_0(z) = 0.07$) calculated from the transient simulation for $Ca = 0.349$, $Q = 0.0063$ and $c_\infty = 1.47$ (symbols). The solid line is the global stability analysis prediction (3.21) ($a_0 = 0.0029$, $t_0 = -2.7$, $\omega_i = -0.0107$ and $\omega_r = 0.519$). The blue and black arrows in the inset show the location of the initial perturbation and the analysed interface point, respectively. The time has been made dimensionless with the inertio-capillary time $t_{ic} = (\rho_i \hat{R}_c^3/\gamma_*)^{1/2}$.

was given by the function

$$F(z, 0) - F_0(z) = \beta\, \mathrm{e}^{-(z-z_0)^2/\Delta z^2}, \tag{6.1}$$

where β indicates the maximum deformation amplitude, while z_0 and Δz are the location and width, respectively. The perturbation amplitude and width are small ($\beta = 5 \times 10^{-4}$ and $\Delta z = 0.5$). The perturbation is introduced next to the feeding capillary ($z_0 - z_e = 0.2$).

The free surface displacement $F(z, t) - F_0(z)$ at the meniscus tip is shown in figure 15. The parameter conditions correspond to a linearly stable flow relatively close to the stability limit ($\omega_i = -0.0107$). The perturbation (6.1) triggers a train of capillary waves propagating downstream. The interface deformation in the meniscus tip becomes noticeable at times of the order of the inertio-capillary time $t_{ic} = (\rho_i \hat{R}_c^3/\gamma_*)^{1/2}$. The perturbation produces an interface oscillation in the meniscus tip much larger than the deformation given by (6.1). In this sense, the base flow behaves as a signal amplifier. However, viscosity slowly dampens the perturbation in this quasi-marginally stable base flow. For sufficiently large t, the contribution of subdominant eigenmodes becomes negligible, and the dominant mode essentially governs the system's linear dynamics. The comparison with the prediction

$$F - F_0 = a_0\, \mathrm{e}^{\omega_i (t-t_0)} \cos[\omega_r (t - t_0)], \tag{6.2}$$

of the global stability analysis shows excellent agreement (figure 15). Here, a_0 and t_0 are fitting parameters, and ω_i and ω_r are the damping rate and frequency of the dominant mode.

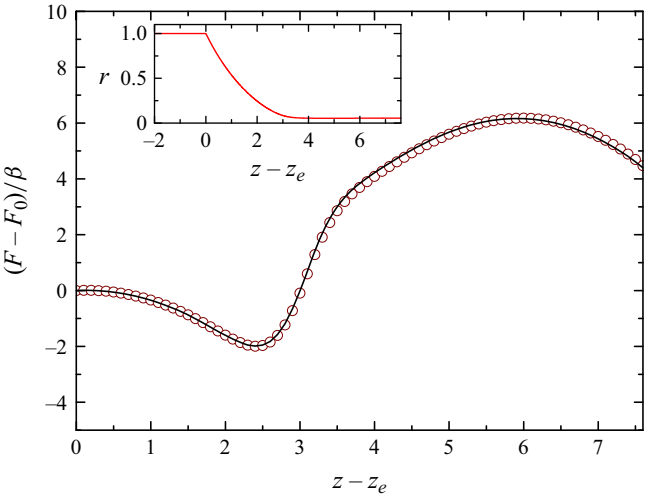

Figure 16. Free surface displacement, $F(z,t)-F_0(z)$, at $t=133$ (in terms of the inertio-capillary time) calculated from the transient simulation for $Ca=0.349$, $Q=0.0063$ and $c_\infty=1.47$ (symbols). The solid line is the deformation (3.21) corresponding to the dominant mode ($t_0=-2.7$ and $\omega=0.519-0.0107\mathrm{i}$). The inset shows the base flow interface location.

The interface deformation at $t=133$ is shown in figure 16. The comparison with the deformation

$$F-F_0=\mathrm{Re}[\delta F\,\mathrm{e}^{-\mathrm{i}\omega(t-t_0)}], \tag{6.3}$$

caused by the dominant mode shows remarkable agreement as well. Here, δF and $\omega=\omega_r+\mathrm{i}\omega_i$ are the deformation amplitude and eigenfrequency of the dominant mode, respectively. The interface deformation is much larger than the initial perturbation given by (6.1) despite the long time (in terms of the inertio-capillary time) lapsed from $t=0$. The maximum interface deformation is reached in the discharge tube due to the strong convective nature of the flow.

The results presented in this section illustrate the usefulness of the global stability analysis. The transient simulations took 20 times longer than the global stability analysis for the same grid. The reduced spatial resolution ($n_\chi^i=n_\chi^o=30$, $n_\xi^{(i)}=n_\xi^{(o)}=3601$) of the transient simulation explains the slight discrepancies with respect to the global stability analysis predictions.

7. Parametric study

This section analyses the surfactant stabilizing effect when a relevant parameter changes. Specifically, we calculate the minimum flow rate ratio Q_{min} as a function of that parameter, while the values of the rest are those defined in § 4.

We have verified that the minimum flow rate is hardly affected by the diffusion coefficient, even if this parameter increases by two orders of magnitude. Specifically, $Q_{min}=0.005$ and 0.0052 for $Pe=5.89\times10^6$ and 5.89×10^4, respectively. This occurs due to the strong surfactant convection, which renders the surfactant volumetric concentration practically constant in the fluid domain, including the sublayer next to the interface (see § 4). We take advantage of this fact and conduct the rest of the parametric study for $Pe=5.89\times10^4$, which allows us to reduce the number of grid points considerably.

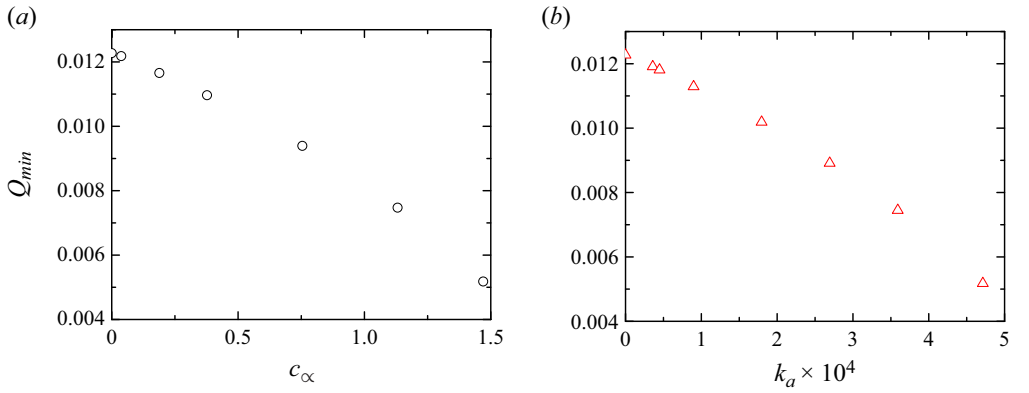

Figure 17. Value of Q_{min} as a function of c_∞ (a) and k_a (b). The values of the rest of the parameters are those specified in § 4.

Surfactant desorption is so small that it has a negligible effect on the flow stability. We have verified that the minimum flow rate does not significantly change when the desorption constant is increased by one order of magnitude with respect to the SDS value.

7.1. *Influence of the surfactant concentration and the adsorption constant*

We analyse the influence of the surfactant concentration c_∞ and adsorption constant k_a in figure 17. As observed in figure 5, $c_\infty = 1.47$ and $k_a = 4.71 \times 10^{-4}$ lead to surfactant surface concentrations relatively close to the maximum packing density in the meniscus tip and the emitted jet. Increasing c_∞ and k_a above those values hinders the numerical method convergence and may render the Langmuir equation of state inaccurate. For this reason, we restrict our analysis to $c_\infty \leq 1.47$ and $k_a \leq 4.71 \times 10^{-4}$.

As expected, the minimum flow rate ratio decreases as the surfactant concentration and adsorption constant increase (figure 17). We find approximately linear dependencies of Q_{min} on c_∞ and k_a within the intervals of those parameters analysed. There is a relatively small effect on the flow stability for, say, $c_\infty \lesssim 0.5$ ($\hat{c}_\infty \lesssim 0.5\hat{c}_{cmc}$). This agrees with experimental results, which indicate that the surfactant concentration must exceed by far the critical micelle concentration to produce noticeable effects (Moyle *et al.* 2012; López *et al.* 2022).

Figure 18 shows the minimum flow rate ratio Q_{min} as a function of $c_\infty k_a$. The circles are the results obtained for $k_a = 4.71 \times 10^{-4}$ and surfactant concentrations c_∞ in the interval $[0, 1.47]$. The triangles are the results obtained for $c_\infty = 1.47$ and adsorption constants k_a in the interval $[0, 4.71 \times 10^{-4}]$. Convection ensures that the volumetric surfactant concentration at the interface approximately equals c_∞. Therefore, $\mathcal{J}_a \simeq k_a c_\infty(1 - \Gamma)$, which means that the amount of surfactant absorbed on the interface is directly proportional to $k_a c_\infty$. For this reason, the microjetting stability depends on c_∞ and k_a through the product $k_a c_\infty$ (figure 18).

Figure 19 shows the excellent agreement between the simulation results and the prediction (4.3) for the jet radius R_j. The symbols correspond to both stable and unstable base flows with and without surfactant. The surfactant monolayer does not affect the jet radius, which approximately scales as $Q^{1/2}$.

7.2. *Influence of the capillary number*

This section closes by analysing the role of the capillary number (figure 20). We do not consider capillary numbers larger than 0.35 because the numerical method fails to

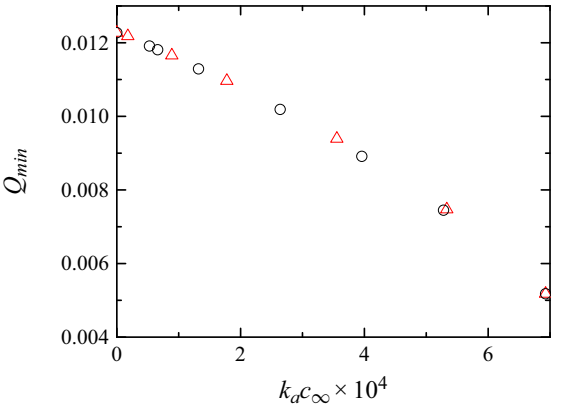

Figure 18. Value of Q_{min} as a function of $k_a c_\infty$. The circles are the results obtained for $k_a = 4.71 \times 10^{-4}$ and surfactant concentrations c_∞ in the interval $[0, 1.47]$. The triangles are the results obtained for $c_\infty = 1.47$ and adsorption constants k_a in the interval $[0, 4.71 \times 10^{-4}]$. The values of the rest of the parameters are those specified in § 4.

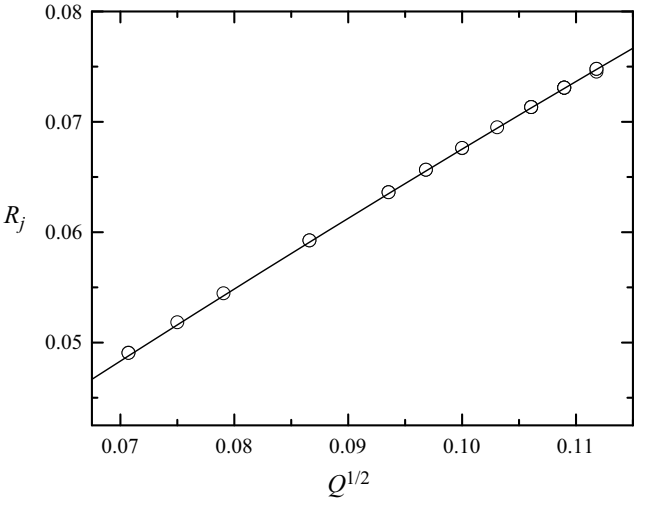

Figure 19. Jet radius R_j as a function of the flow rate ratio Q for the simulations in figure 18. The symbols are the simulation results, while the solid line is the prediction (4.3).

converge to the solution in the presence of the surfactant. This probably occurs because the value $\Gamma = 1$ is exceeded at some interface point during the simulations. As expected, Q_{min} decreases as Ca increases both with and without surfactant. For a given microfluidic device and liquid–liquid system, the increase in capillary number is produced by an increase in the outer flow rate. One may wonder whether the decrease in the flow rate ratio Q_{min} is only due to the increase of Q_o or, conversely, because Q_i decreases as well. The flow rate ratio Q_{min} can be calculated as a function of the inner flow rate as

$$Q_{min} = \frac{4\mu_o Q_i}{\pi \hat{D}^2 \gamma_*} Ca^{-1}. \tag{7.1}$$

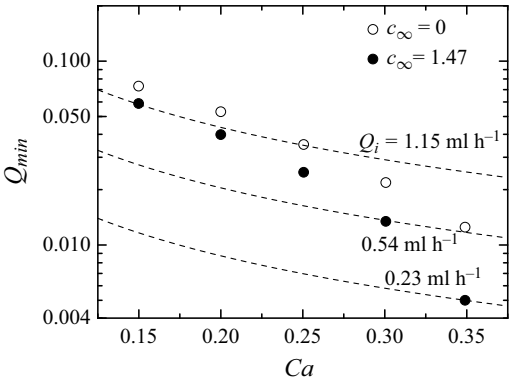

Figure 20. Value of Q_{min} as a function of Ca with (solid symbols) and without (open symbols) surfactant. The dashed lines are the isolines of Q_i. The values of the rest of the parameters are those specified in § 4.

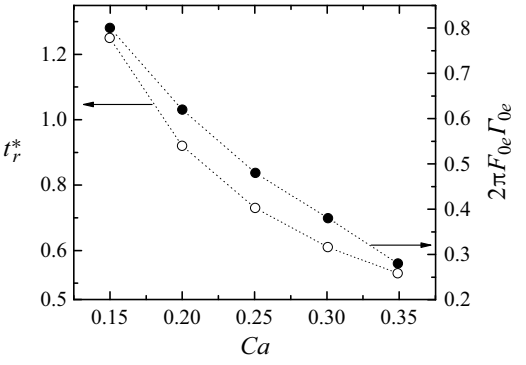

Figure 21. Residence time t_r^* (open symbols) and surfactant carried by the jet per unit length, $2\pi F_{0e}\Gamma_{0e}$, at the numerical domain exit (solid symbols) as a function of Ca. The residence time has been made dimensionless using the adsorption characteristic time $\hat{t}_a = \hat{\Gamma}_\infty/(\hat{k}_a\hat{c}_\infty)$; i.e. $t_r^* = t_r(\hat{R}_c\mu_i/\hat{\gamma}_*)/\hat{t}_a$.

Figure 20 shows three isolines of Q_i for the values of μ_o, $\hat{D}$ and γ_* mentioned § 4. Increasing the capillary number (the outer flow rate) decreases the critical inner flow rate. This behaviour differs from that of gaseous flow focusing, in which the minimum inner flow rate hardly depends on the driving force intensity for sufficiently large values of that quantity (Acero *et al.* 2012).

The interface velocity increases with the capillary number (4.5), which entails the reduction of the residence time

$$t_r = \int_{z_e}^{L_n - z_e} \frac{(1 + F_{0z}^2)^{1/2}}{v_0^s}\,\mathrm{d}z, \tag{7.2}$$

of the interface element in the numerical domain. Figure 21 shows the residence time and the surfactant transported by the jet per unit length, $2\pi F_{0e}\Gamma_{0e}$, where F_{0e} and Γ_{0e} are the jet radius and surfactant surface concentration evaluated at the numerical domain exit, respectively. The decrease in the residence time reduces the amount of surfactant carried by the jet.

As mentioned in § 4, the interface element area drastically decreases in the meniscus tip, which increases the surfactant surface concentration. This effect is more noticeable as Ca increases due to the decrease in Q_{min} (and therefore R_j) (figure 20). In fact, $\hat{\Gamma} \simeq \hat{\Gamma}_\infty$

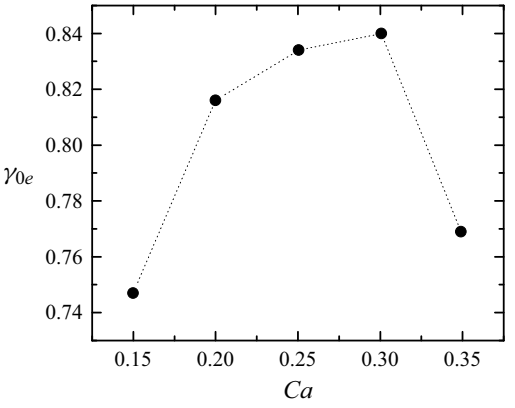

Figure 22. Jet surface tension γ_{0e} at the numerical domain exit as a function of Ca.

($\Gamma \simeq 1$) at the meniscus tip for $Ca = 0.349$ (figure 5) even though the residence time in terms of the adsorption characteristic time, $\hat{t}_a = \hat{\Gamma}_\infty/(\hat{k}_a\hat{c}_\infty)$, is much smaller than unity (figure 21). The competition between the residence time and surface contraction explains the non-monotonic dependency of the jet surface tension (surfactant surface concentration) on the capillary number (figure 22).

The surfactant stabilizing effect increases with the capillary number. Specifically, the relative reduction of Q_{min} for $c_\infty = 1.47$ monotonically increases with Ca (figure 20). This contrasts the non-monotonic dependency of the jet surface tension on the capillary number discussed above (figure 22). For $Ca \leq 0.3$, the surfactant stabilizing effect increases with Ca (figure 20) even though the jet surface tension increases with Ca (figure 21). This contradicts the common assumption that adding surfactant favours tip streaming simply because it reduces the meniscus tip surface tension.

8. Conclusions

We have numerically analysed the effect of a soluble surfactant on the microjetting mode of the liquid–liquid flow focusing configuration. The surfactant is convected across a very narrow annular streamtube next to the interface and adsorbs on the interface next to the feeding capillary. Convection renders the surfactant concentration relatively constant throughout the fluid domain. The increase in the surfactant surface concentration in front of the emitted jet significantly reduces the surface tension there. The resulting Marangoni stress in the meniscus tip substantially alters the balance of the tangential stresses at the interface but does not reduce the interface velocity. For this reason, the base flows with and without surfactant are similar on the scale given by the feeding capillary radius. The surfactant significantly reduces the meniscus tip capillary pressure opposing the flow.

The global stability analysis at the minimum flow rate stability limit shows that both the Marangoni stress and soluto-capillarity in the meniscus tip contribute to flow stabilization. Our analysis allows us to distinguish the surfactant stabilizing effect through the perturbations and the base flow. The surface tension perturbation caused by the critical mode induces both pressure-driven and Marangoni flows that oppose the growth of that mode, which explains the major stabilizing effect of the surfactant monolayer. In addition, the accumulation of surfactant in the meniscus tip reduces the adverse capillary pressure gradient in the base flow, which may contribute to stabilizing the microjetting mode.

Surfactant diffusion and desorption hardly affect the stability limit. Noticeable effects are observed only for concentrations well above the critical micelle concentration. Due to the surfactant convection, the concentration at the interface is approximately the same as that in the liquid reservoir c_∞. This explains why the minimum flow rate ratio depends on the adsorption constant k_a and the surfactant concentration c_∞ through the product $k_a c_\infty$. The stabilizing effect of the surfactant monolayer increases with the capillary number (the outer flow rate). Interestingly, the magnitude of the surfactant stabilizing effect can increase even when the jet surface tension increases.

We have theoretically demonstrated that surfactants can considerably stabilize the microjetting mode of liquid–liquid flow focusing. This stabilization entails significantly reducing the minimum jet diameter obtained with this technique. Therefore, using surfactants in hydrodynamic focusing not only stabilizes the microemulsion resulting from the jet breakup but also reduces the droplet size. The surfactant monolayer hardly influences the non-critical (subdominant) linear eigenmodes but significantly alters the critical one. This mode perturbs the surface tension distribution over the interface, producing a Marangoni stress that contributes to stabilizing the flow.

In our simulations, the surfactant was added to the inner phase. We do not expect significant differences when the surfactant is dissolved in the outer fluid. The scaling analysis in § 4 also applies to that case. The fact that the outer viscosity is larger than the inner one does not alter the conclusion: the surfactant concentration on the outer side of the interface practically equals that of the liquid reservoir. Therefore, the surfactant transfer from the outer liquid to the interface is essentially the same as when the surfactant is present in the inner phase. It is natural to hypothesize that the base flow and its response to perturbations are practically the same when the surfactant is dissolved in the inner and outer fluids.

Funding. This research has been supported by the Spanish Ministry of Economy, Industry and Competitiveness under grants PID2019-108278RB, PID2022-140951OB-C21 and PID2022-140951OB-C22/AEI/10.13039/501100011033/FEDER,UE.

Declaration of interests. The authors report no conflict of interest.

Author ORCIDs.
M. Rubio https://orcid.org/0000-0002-2380-9545;
M.G. Cabezas https://orcid.org/0000-0002-9126-2254;
J.M. Montanero https://orcid.org/0000-0002-3906-5931;
M.A. Herrada https://orcid.org/0000-0003-0388-8001.

Appendix. Separate effects of soluto-capillarity and Marangoni stress on the perturbations

In the presence of the surfactant, the perturbation amplitude δF of the interface location peaks at the meniscus-to-jet transition, as shown by the black line in figure 23. This suggests that the instability originates in that region. For this reason, we pay attention to the effects of soluto-capillarity and Marangoni stresses there.

In the presence of a surfactant monolayer, the surface tension variation $\delta\gamma$ produces an extra capillary pressure variation $\delta p_\gamma = \delta\gamma\kappa_0$ that does not exist when the surface tension is constant (see § 5.2). This variation drives the inner liquid from regions with higher values of δp_γ to those with lower values of this quantity (figure 23). The analysis of δp_γ alone is inconclusive. The real and imaginary parts of δF and δp_γ show that δp_γ drives the inner liquid from the right side of the perturbation neck (i.e. where $\mathrm{Re}[\delta F]$ and $\mathrm{Im}[\delta F]$ are minimum) towards the neck. This is a stabilizing effect because it opposes the neck

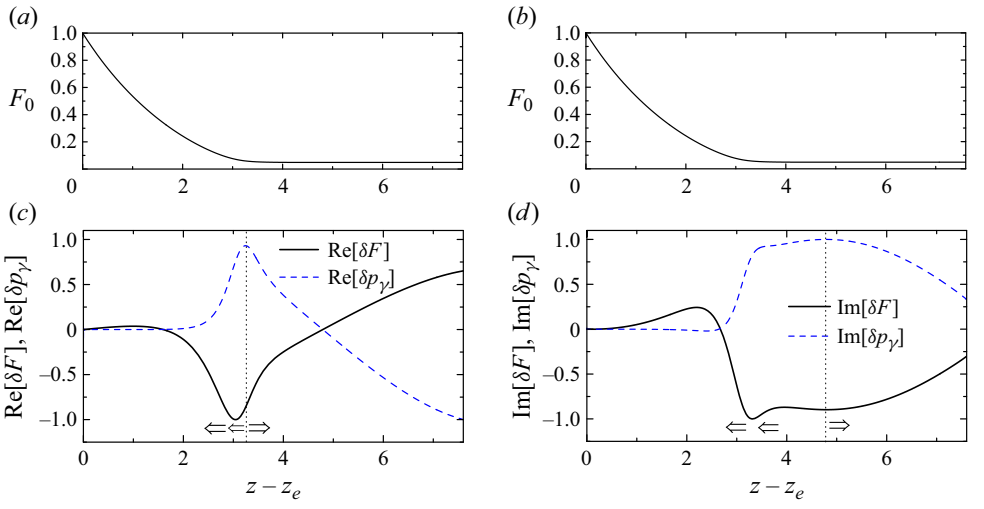

Figure 23. Interface location $F_0(z)$, (a,b) perturbation of the interface location $\delta F(z)$ and perturbation of the capillary pressure δp_γ (c,d). The results correspond to the critical mode for $Ca = 0.349$, $Q = 0.005$ and $c_\infty = 1.470$. The values of δF (δp_γ) are normalized by dividing them by the absolute value of the minimum (maximum) value, respectively. The minimum values of Re[δF] and Im[δF] are -0.880×10^{-5} and -0.548×10^{-5}, respectively, while the maximum values of Re[δp] and Im[δp] are 0.163×10^{-2} and 0.171×10^{-2}, respectively. The dotted line indicates the maximum of δp_γ. The arrows indicate the direction of the flow associated with δp_γ.

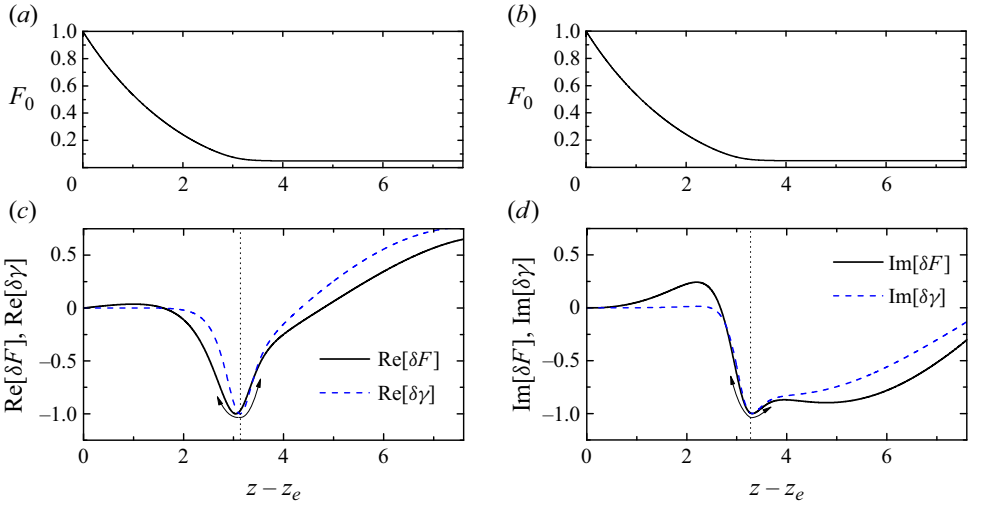

Figure 24. Interface location $F_0(z)$ (a,b), perturbation of the interface location $\delta F(z)$ and perturbation of the surface tension $\delta\gamma$ (c,d). The results correspond to the critical mode for $Ca = 0.349$, $Q = 0.005$ and $c_\infty = 1.470$. The values of δF and $\delta\gamma$ are normalized by dividing them by the absolute value of the corresponding minimum value. The minimum values of Re[δF] and Im[δF], Re[δp] and Im[δp] are -0.880×10^{-5}, -0.548×10^{-5}, -0.119×10^{-4} and -0.104×10^{-4}, respectively. The dotted line indicates the minimum of $\delta\gamma$. The arrows indicate the direction of flow associated with $\delta\tau_*^{Ma}$.

thinning. However, the opposite effect is observed on the left side of the neck. These results, combined with those in figure 12, suggest that the flow towards the perturbation neck stabilizes the base flow.

The surface tension variation $\delta\gamma$ also produces a Marangoni stress $\delta\tau_*^{Ma} = -\delta\gamma_z(1 + F_{0z}^2)^{1/2}$, as explained in § 5.2. This stress drives the inner liquid from regions with lower surface tension (smaller values of $\delta\gamma$) to those with higher values of this quantity (larger values of $\delta\gamma$). One expects the Marangoni stress to dampen the perturbation if it drives the liquid towards the neck of the interface perturbation $\delta F(z)$, opposing the neck thinning.

Figure 24 shows the flow induced by the Marangoni stress perturbation $\delta\tau_*^{Ma}$. The real parts of δF and $\delta\gamma$ show that the Marangoni stress drives the inner liquid from the right side of the perturbation neck towards the neck (figure 24*a*,*c*). However, the opposite effect is observed on the left side of the neck. The imaginary parts of δF and $\delta\gamma$ show a destabilizing effect because the Marangoni stress drags the inner phase from the perturbation neck (figure 24*b*,*d*). Therefore, it is unclear from figure 24 whether the Marangoni convection caused by $\delta\Gamma(z)$ plays a stabilizing or destabilizing role. Nevertheless, these results combined with those in figure 12 indicate that the reverse flow towards the perturbation neck dragged by $\delta\tau_*^{Ma}$ during part of the oscillation causes a net stabilizing effect. This effect resembles the stabilizing mechanism responsible for the end-pinching escape of a surfactant-laden liquid thread (Kamat *et al.* 2020).

References

Acero, A.J., Ferrera, C., Montanero, J.M. & Gañán-Calvo, A.M. 2012 Focusing liquid microjets with nozzles. *J. Micromech. Microengng* **22**, 065011.

Anna, S.L. 2016 Droplets and bubbles in microfluidic devices. *Annu. Rev. Fluid Mech.* **48**, 285–309.

Anna, S.L., Bontoux, N. & Stone, H.A. 2003 Formation of dispersions using flow focusing in microchannels. *Appl. Phys. Lett.* **82**, 364–366.

Baret, J.-C. 2012 Surfactants in droplet-based microfluidics. *Lab on a Chip* **12**, 422–433.

Booty, M.R. & Siegel, M. 2005 Steady deformation and tip-streaming of a slender bubble with surfactant in an extensional flow. *J. Fluid Mech.* **544**, 243–275.

Cabezas, M.G., Rubio, M., Rebollo-Muñoz, N., Herrada, M.A. & Montanero, J.M. 2021 Global stability analysis of axisymmetric liquid-liquid flow focusing. *J. Fluid Mech.* **909**, A10.

Chang, C.-H. & Franses, E.I. 1995 Adsorption dynamics of surfactants at the air/water interface: a critical review of mathematical models, data, and mechanisms. *Colloids Surf.* A **100**, 1–45.

Christopher, G.F. & Anna, S.L. 2007 Microfluidic methods for generating continuous droplet streams. *J. Phys.* D*: Appl. Phys.* **40**, R319–R336.

Cohen, I. 2004 Scaling and transition structure dependence on the fluid viscosity ratio in the selective withdrawal transition. *Phys. Rev.* E **70**, 026302.

Cohen, I., Li, H., Hougland, J.L., Mrksich, M. & Nagel, S.R. 2001 Using selective withdrawal to coat microparticles. *Science* **292**, 265–267.

Craster, R.V., Matar, O.K. & Papageorgiou, D.T. 2009 Breakup of surfactant-laden jets above the critical micelle concentration. *J. Fluid Mech.* **629**, 195–219.

Cruz-Mazo, F., Herrada, M.A., Gañán-Calvo, A.M. & Montanero, J.M. 2017 Global stability of axisymmetric flow focusing. *J. Fluid Mech.* **832**, 329–344.

De Bruijn, R.A. 1993 Tipstreaming of drops in simple shear flows. *Chem. Engng Sci.* **48**, 277–284.

Dimakopoulos, Y. & Tsamopoulos, J. 2003 A quasi-elliptic transformation for moving boundary problems with large anisotropic deformations. *J. Comput. Phys.* **192**, 494–522.

Eggleton, C.D., Tsai, T.-M. & Stebe, K.J. 2001 Tip streaming from a drop in the presence of surfactants. *Phys. Rev. Lett.* **87**, 048302.

Evangelio, A., Campo-Cortés, F. & Gordillo, J.M. 2016 Simple and double microemulsions via the capillary breakup of highly stretched liquid jets. *J. Fluid Mech.* **804**, 550–577.

Frumkin, A. & Levich, V. 1947 On surfactants an interfacial motion (in Russian). *Zhur. Fiz. Khim.* **21**, 1183.

Gañán-Calvo, A.M., González-Prieto, R., Riesco-Chueca, P., Herrada, M.A. & Flores-Mosquera, M. 2007 Focusing capillary jets close to the continuum limit. *Nat. Phys.* **3**, 737–742.

GAÑÁN-CALVO, A.M. & RIESCO-CHUECA, P. 2006 Jetting-dripping transition of a liquid jet in a lower viscosity co-flowing immiscible liquid: the minimum flow rate in flow focusing. *J. Fluid Mech.* **553**, 75–84.

GORDILLO, J.M., SEVILLA, A. & CAMPO-CORTÉS, F. 2014 Global stability of stretched jets: conditions for the generation of monodisperse micro-emulsions using coflows. *J. Fluid Mech.* **738**, 335–357.

HE, K., CAMPO-CORTÉS, F., GORAL, M., LÓPEZ-LEÓN, T. & GORDILLO, J.M. 2019 Micron-sized double emulsions and nematic shells generated via tip streaming. *Phys. Rev. Fluids* **4**, 124201.

HE, Y., YAZHGUR, P., SALONEN, A. & LANGEVIN, D. 2015 Adsorption–desorption kinetics of surfactants at liquid surfaces. *Adv. Colloid Interface Sci.* **222**, 377–384.

HERRADA, M.A. 2023 This method has recently been termed JAM (Jacobian Analytical Method). Examples of JAM codes can be found at https://github.com/miguelherrada/JAM.

HERRADA, M.A. & MONTANERO, J.M. 2016 A numerical method to study the dynamics of capillary fluid systems. *J. Comput. Phys.* **306**, 137–147.

HERRADA, M.A., PONCE-TORRES, A., RUBIO, M., EGGERS, J. & MONTANERO, J.M. 2022 Stability and tip streaming of a surfactant-loaded drop in an extensional flow. influence of surface viscosity. *J. Fluid Mech.* **934**, A26.

HUERRE, P. & MONKEWITZ, P.A. 1990 Local and global instabilites in spatially developing flows. *Annu. Rev. Fluid Mech.* **22**, 473–537.

KALOGIROU, A. & BLYTH, M.G. 2019 The role of soluble surfactants in the linear stability of two-layer flow in a channel. *J. Fluid Mech.* **873**, 18–48.

KAMAT, P.M., WAGONER, B.W., CASTREJÓN-PITA, A.A., CASTREJÓN-PITA, J.R., ANTHONY, C.R. & BASARAN, O.A. 2020 Surfactant-driven escape from endpinching during contraction of nearly inviscid filaments. *J. Fluid Mech.* **899**, A28.

KHORRAMI, M.R. 1989 Application of spectral collocation techniques to the stability of swirling flows. *J. Comput. Phys.* **81**, 206–229.

LANGEVIN, D. 2014 Rheology of adsorbed surfactant monolayers at fluid surfaces. *Annu. Rev. Fluid Mech.* **46**, 4765.

LEE, W., WALKER, L.M. & ANNA, S.L. 2011 Competition between viscoelasticity and surfactant dynamics in flow focusing microfluidics. *Macromol. Mater. Engng* **296**, 203–213.

LEVICH, V.G. 1962 *Physicochemical Hydrodynamics*. Prentice-Hall.

LI, J. & MANIKANTAN, H. 2024 Stability and thinning of liquid jets in the presence of soluble surfactants. *J. Chem. Phys.* **160**, 024902.

LIANG, X., LI, M., WANG, K. & LUO, G. 2022 Determination of time-evolving interfacial tension and ionic surfactant adsorption kinetics in microfluidic droplet formation process. *J. Colloid Interface Sci.* **617**, 106–117.

LÓPEZ, M., CABEZAS, M.G., MONTANERO, J.M. & HERRADA, M.A. 2022 On the hydrodynamic focusing for producing microemulsions via tip streaming. *J. Fluid Mech.* **934**, A47.

LYTRA, A., VLACHOMITROU, M. & PELEKASIS, N. 2024 Numerical study of the steady core-annular flow in a focusing geometry in the presence of soluble surfactants. *Intl J. Multiphase Flow* **170**, 104652.

MARÍN, A.G., CAMPO-CORTÉS, F. & GORDILLO, J.M. 2009 Generation of micron-sized drops and bubbles through viscous coflows. *Colloids Surf.* A*: Physicochem. Engng Aspects* **344**, 2–7.

MARTÍNEZ-CALVO, A. & SEVILLA, A. 2020 Universal thinning of liquid filaments under dominant surface forces. *Phys. Rev. Lett.* **125**, 114502.

MONTANERO, J.M. & GAÑÁN-CALVO, A.M. 2020 Dripping, jetting and tip streaming. *Rep. Prog. Phys.* **83**, 097001.

MOYLE, T.M., WALKER, L.M. & ANNA, S.L. 2012 Predicting conditions for microscale surfactant mediated tipstreaming. *Phys. Fluids* **24**, 082110.

PONCE-TORRES, A., REBOLLO-MUÑOZ, N., HERRADA, M.A., GAÑÁN-CALVO, A.M. & MONTANERO, J.M. 2018 The steady cone-jet mode of electrospraying close to the minimum volume stability limit. *J. Fluid Mech.* **857**, 142–172.

PONCE-TORRES, A., RUBIO, M., HERRADA, M.A., EGGERS, J. & MONTANERO, J.M. 2020 Influence of the surface viscous stress on the pinch-off of free surfaces loaded with nearly-inviscid surfactants. *Sci. Rep.* **10**, 16065.

RAYLEIGH, LORD 1878 On the instability of jets. *Proc. Lond. Math. Soc.* **s1-10**, 4–13.

ROSEN, M.J. 2004 *Surfactants and Interfacial Phenomena*. John Wiley and Sons.

RUBIO, M., MONTANERO, J.M., EGGERS, J. & HERRADA, M.A. 2024 Stable production of fluid jets with vanishing diameters via tip streaming. *J. Fluid Mech.* **984**, A4.

RUBIO-RUBIO, M., SEVILLA, A. & GORDILLO, J.M. 2013 On the thinnest steady threads obtained by gravitational stretching of capillary jets. *J. Fluid Mech.* **729**, 471–483.

SURYO, R. & BASARAN, O.A. 2006 Tip streaming from a liquid drop forming from a tube in a co-flowing outer fluid. *Phys. Fluids* **18**, 082102.

THEOFILIS, V. 2011 Global linear instability. *Annu. Rev. Fluid Mech.* **43**, 319–352.

TOMOTIKA, S. 1935 On the instability of a cylindrical thread of a viscous liquid surrounded by another viscous fluid. *Proc. R. Soc. Lond.* **150**, 322–337.

TRICOT, Y.-M. 1997 Surfactants: static and dynamic surface tension. In *Liquid Film Coating*, vol. 1, pp. 100–136. Chapman and Hall.

WANG, Q., SIEGEL, M. & BOOTY, M.R. 2014 Numerical simulation of drop and bubble dynamics with soluble surfactant. *Phys. Fluids* **26**, 052102.

WEE, H., WAGONER, B.W., KAMAT, P.M. & BASARAN, O.A. 2020 Effects of surface viscosity on breakup of viscous threads. *Phys. Rev. Lett.* **124**, 204501.

WROBEL, J.K., BOOTY, M.R., SIEGEL, M. & WANG, Q. 2018 Simulation of surfactant-mediated tipstreaming in a flow-focusing geometry. *Phys. Rev. Fluids* **3**, 114003.

ZELL, Z.A., NOWBAHAR, A., MANSARD, V., LEAL, L.G., DESHMUKH, S.S., MECCA, J.M., TUCKER, C.J. & SQUIRES, T.M. 2014 Surface shear inviscidity of soluble surfactants. *Proc. Natl Acad. Sci.* **111**, 3677–3682.